UC Irvine
UC Irvine Previously Published Works

Title
The Effect of Host Star Spectral Energy Distribution and Ice-Albedo Feedback on the Climate of Extrasolar Planets

Permalink
https://escholarship.org/uc/item/0rz1r6c8

Journal
Astrobiology, 13(8)

ISSN
1531-1074

Authors
Shields, Aomawa L
Meadows, Victoria S
Bitz, Cecilia M
et al.

Publication Date
2013-08-01

DOI
10.1089/ast.2012.0961

Copyright Information
This work is made available under the terms of a Creative Commons Attribution License, availalbe at https://creativecommons.org/licenses/by/4.0/

Peer reviewed

eScholarship.org Powered by the California Digital Library
University of California

ASTROBIOLOGY
Volume 13, Number 8, 2013
© Mary Ann Liebert, Inc.
DOI: 10.1089/ast.2012.0961

The Effect of Host Star Spectral Energy Distribution and Ice-Albedo Feedback on the Climate of Extrasolar Planets

Aomawa L. Shields,[1,2,3] Victoria S. Meadows,[2,3] Cecilia M. Bitz,[4]
Raymond T. Pierrehumbert,[5] Manoj M. Joshi,[6] and Tyler D. Robinson[2,3]

Abstract

Planetary climate can be affected by the interaction of the host star spectral energy distribution with the wavelength-dependent reflectivity of ice and snow. In this study, we explored this effect with a one-dimensional (1-D), line-by-line, radiative transfer model to calculate broadband planetary albedos as input to a seasonally varying, 1-D energy balance climate model. A three-dimensional (3-D) general circulation model was also used to explore the atmosphere's response to changes in incoming stellar radiation, or instellation, and surface albedo. Using this hierarchy of models, we simulated planets covered by ocean, land, and water-ice of varying grain size, with incident radiation from stars of different spectral types. Terrestrial planets orbiting stars with higher near-UV radiation exhibited a stronger ice-albedo feedback. We found that ice extent was much greater on a planet orbiting an F-dwarf star than on a planet orbiting a G-dwarf star at an equivalent flux distance, and that ice-covered conditions occurred on an F-dwarf planet with only a 2% reduction in instellation relative to the present instellation on Earth, assuming fixed CO_2 (present atmospheric level on Earth). A similar planet orbiting the Sun at an equivalent flux distance required an 8% reduction in instellation, while a planet orbiting an M-dwarf star required an additional 19% reduction in instellation to become ice-covered, equivalent to 73% of the modern solar constant. The reduction in instellation must be larger for planets orbiting cooler stars due in large part to the stronger absorption of longer-wavelength radiation by icy surfaces on these planets in addition to stronger absorption by water vapor and CO_2 in their atmospheres, which provides increased downwelling longwave radiation. Lowering the IR and visible-band surface ice and snow albedos for an M-dwarf planet increased the planet's climate stability against changes in instellation and slowed the descent into global ice coverage. The surface ice-albedo feedback effect becomes less important at the outer edge of the habitable zone, where atmospheric CO_2 could be expected to be high such that it maintains clement conditions for surface liquid water. We showed that $\sim$3–10 bar of CO_2 will entirely mask the climatic effect of ice and snow, leaving the outer limits of the habitable zone unaffected by the spectral dependence of water ice and snow albedo. However, less CO_2 is needed to maintain open water for a planet orbiting an M-dwarf star than would be the case for hotter main-sequence stars. Key Words: Extrasolar planets—M stars—Habitable zone—Snowball Earth. Astrobiology 13, 715–739.

1. Introduction

M-dwarf stars are believed to comprise $\sim$75% of all main-sequence stars; therefore, they offer the best chance to find orbiting habitable planets through sheer numbers alone. M-dwarf hosts also demonstrate clear advantages for planetary habitability. Because of their small masses compared to the Sun (0.08–0.5 $M_{\odot}$), M-dwarf stars burn nuclear fuel at a much slower rate and are therefore extremely long-lived, offering lengthy timescales for planetary and biological evolution. Earth-sized planets around M-dwarf stars are easier to detect with existing techniques, since

[1]Department of Astronomy, University of Washington, Seattle, Washington, USA.
[2]Department of Astronomy and Astrobiology Program, University of Washington, Seattle, Washington, USA.
[3]NASA Astrobiology Institute.
[4]Department of Atmospheric Sciences, University of Washington, Seattle, Washington, USA.
[5]Department of Geological Sciences, University of Chicago, Chicago, Illinois, USA.
[6]School of Environmental Sciences, University of East Anglia, Norwich, Norfolk, UK.

both stellar radial velocity and photometric transit depths are larger given the lower star-to-planet mass and size ratios (Tarter *et al.*, 2007). Because of the lower luminosities of M dwarfs, their habitable zones (defined as the locus of orbits around a star where an Earth-like planet can support liquid water on its surface, Kasting *et al.*, 1993) will be much closer to the star (0.24–0.44 AU for an early-type M dwarf, assuming an effective temperature of 3800 K and luminosity of 0.05 $L_{\odot}$, Kopparapu *et al.*, 2013a, 2013b) than habitable zones of G-dwarf stars like the Sun (0.99–1.67 AU, Kopparapu *et al.*, 2013a, 2013b), increasing the geometric probability of observing a transit, which scales inversely with a planet's orbital distance from its host star (Borucki and Summers, 1984).

A planet orbiting an M-dwarf star (henceforth called an M-dwarf planet) would experience a very different environment from that of a planet orbiting a larger, brighter star. In such close-in orbits, tidal effects are expected to be strong and could lead to synchronous rotation, where the planet takes as long to make one rotation as it does to complete one orbit around its star (Dole, 1964; Kasting *et al.*, 1993; Joshi *et al.*, 1997; Edson *et al.*, 2011). Previous work suggests that aqua planets cool with increasing rotation period due to weakened low-latitude zonal winds that allow sea ice to expand across the planet (Edson *et al.*, 2011). Initial concerns about M-dwarf planet atmospheres condensing out on the permanent nightside were assuaged by climate simulations of synchronously rotating M-dwarf planets, which suggest that 0.1 bar of a gas such as CO_2 is enough to ensure sufficient heat transport between the sunlit and dark sides of the planet and prevent atmospheric freeze-out (Joshi *et al.*, 1997; Edson *et al.*, 2011). Edson *et al.* (2011) also found that increased atmospheric latent and oceanic diffusive heat transport reduced temperature contrasts between the sunlit and dark sides of an aqua planet. M-dwarf stars also exhibit high degrees of chromospheric activity, which results in flares that emit significant amounts of high-energy radiation (Hawley and Pettersen, 1991) that could be detrimental to surface life. However, photochemical and radiative-convective models have yielded a maximum depletion in atmospheric ozone number density of 1% due to UV radiation emitted by flares, indicating that planetary surface habitability may not be unequivocally threatened by stellar flare events. The addition into simulations of the proton flux that can be associated with stellar flares results in a reduction in ozone column depth by as much as 93%. This is an upper limit, as not all flares are accompanied by the ejection of energetic ionizing particles, and the effect of flare-associated particle ejections on atmospheric ozone concentration could be ameliorated by a planet's magnetic field (Segura *et al.*, 2010).

M-dwarf stars emit a large fraction of their radiation at near-IR wavelengths, which can strongly affect planetary climate. About 95% of the radiation emitted by the M-dwarf star AD Leo is at wavelengths longer than 0.7 μm, compared to $\sim$53% for the Sun. Given the dependence of ice and snow albedo on wavelength, the interaction between the spectral energy distribution (SED) of M-dwarf stars and the icy or snowy surfaces that may exist on their orbiting planets will also differ greatly from that of other host stars and their planets' ice surfaces. In the near-UV ($0.3\,\mu\text{m} < \lambda < 0.4\,\mu\text{m}$) and visible ($0.4\,\mu\text{m} \leq \lambda \leq 0.7\,\mu\text{m}$) range of the electromagnetic spectrum, both ice and snow albedo are high, while in the IR and near IR ($\lambda > 0.7\,\mu\text{m}$), the reflectance of ice and snow drops substantially due to an increase in their absorption coefficients at longer wavelengths (Dunkle and Bevans, 1956), a consequence in large part of molecular vibrations involving various combinations of the water molecule's three fundamental vibrational modes (Farrell and Newnham, 1967). Because of the spectral dependence of ice albedo, the ice-albedo feedback mechanism is sensitive to the wavelength of light coming from the host star. On M-dwarf planets, a significant amount of radiation emitted by the host star is absorbed by atmospheric gases such as CO_2 and water vapor, which absorb strongly in the near IR (Kasting *et al.*, 1993; Selsis *et al.*, 2007). However, a disproportionate amount of the longer-wavelength radiation that does reach the surface will be absorbed by, rather than reflected from, icy or snowy surfaces on these planets (Joshi and Haberle, 2012). This will reduce the difference between ice and ocean surface albedo. Episodes of low-latitude glaciation, termed "Snowball Earth" events (Kirschvink, 1992) may be less likely to occur on M-dwarf planets as a result of the lower-albedo ice on their surfaces, as entrance and exit into such a snowball state has been shown to be sensitive to ocean-ice albedo contrast (Pierrehumbert *et al.*, 2011).

Initial work in this area has been of a purely analytical nature, using synthetic stellar and blackbody spectra, one surface water-ice type, and one snow type to show that broadband albedos are likely lower for M-dwarf planets (Joshi and Haberle, 2012). Neither radiative transfer through an atmosphere nor the effect of clouds was included in these calculations. The effect of near-IR CO_2 and water-vapor absorption was estimated by using a constant scaling factor at wavelengths beyond 1.5 μm. Here, we provide a more comprehensive study of this phenomenon, using a hierarchical approach. We use a line-by-line, radiative transfer model that is 1-D in altitude (Meadows and Crisp, 1996; Crisp, 1997), an energy balance model (EBM) that is 1-D in latitude (North and Coakley, 1979), and a 3-D general circulation model (GCM) with both horizontal and vertical spatial resolution (Gent *et al.*, 2011). We also use wavelength-dependent albedo spectra for five different surface ice and snow types across the full near-UV through near-IR range (Grenfell *et al.*, 1994; Warren *et al.*, 2002), with empirical stellar spectra for F-, G-, K-, and M-dwarf stars (Segura *et al.*, 2003, 2010; Chance and Kurucz, 2010).

Historically, the inner and outer edges of the habitable zone (henceforth the IHZ and OHZ) are often defined by the boundary conditions of the runaway greenhouse and the planetary orbital distance beyond which an increase in atmospheric CO_2 concentration is no longer sufficient to maintain surface temperatures above the freezing point of water, termed the maximum CO_2 greenhouse (Kasting *et al.*, 1993; Underwood *et al.*, 2003; Pierrehumbert, 2010; Kane and Gelino, 2012; Kopparapu *et al.*, 2013a). Joshi and Haberle (2012) speculated that the OHZ, which they define as the orbital distance at which carbon dioxide condenses out onto the surface of a planet, may be as much as 30% farther out for M-dwarf stars than originally calculated, given the spectral dependence of water ice and snow albedo. However, at the very outer limit of the habitable zone, atmospheric CO_2 content is expected to be high as a result of decreased silicate weathering (Walker *et al.*, 1981). As the maximum greenhouse limit for CO_2 (more than $\sim$2 bar, Pierrehumbert, 2010) is approached, planetary albedo becomes dominated by the

thicker CO_2 atmosphere and can reduce climate sensitivity to surface ice albedo. The exact CO_2 concentration required to mask the climatic effect of the interaction between host star SED and surface ice and snow has not been constrained, and we determined it here.

The wavelength dependence of ice and snow albedo has been derived analytically, assuming diffuse solar irradiation (Dunkle and Bevans, 1956). Subsequent model comparisons with field measurements have verified the spectral behavior of ice and snow albedo and highlighted its dependence on directional irradiation and solar zenith angle, as well as grain size, with absorption and forward scattering of radiation increasing for larger grains (Wiscombe and Warren, 1980). Here, we explored a large parameter space of possible ice grain sizes and densities to examine the effect of these surface types on planetary climate.

In subsequent sections, we show how we calculated the effect of stellar SED on planetary climate, using a three-tiered approach. First, we used a 1-D radiative transfer model, the Spectral Mapping Atmospheric Radiative Transfer model (SMART), to investigate the interaction between the spectrum of a host star and that of multiple ice types, land, and ocean on a planet orbiting the star at the distance at which it receives an equivalent amount of flux as Earth receives from the Sun (hereafter "equivalent flux distance"). Second, we used a 1-D EBM with our SMART-derived broadband planetary albedos as input to examine the effect of the interaction between the host star's incident radiation (hereafter "instellation") and the latitudinal distribution of surface temperature and ice extent, as a function of the energy balance of the planet. Lastly, we employed a more sophisticated, 3-D GCM to explore the response of the atmosphere and its interaction with the ocean, given the SED of the host star. We also used the 3-D GCM to confirm general trends implied by our EBM simulations and constrain the effect of the spectral dependence of surface water ice and snow albedo on planetary climate. For all model simulations, we assumed a rotation period similar to that of Earth to isolate the effects of SED on planetary climate. As M-dwarf planets are eventually likely to become synchronously rotating (Dole, 1964; Kasting *et al.*, 1993; Joshi *et al.*, 1997; Edson *et al.*, 2011), we look forward to exploring this effect in future work.

2. Models

Here, we describe our method of using a 1-D radiative transfer model to calculate broadband planetary albedos, assuming different incident stellar spectra, a wide range of ice and snow surface types, and land and ocean as input to a seasonally varying, 1-D EBM. With the EBM, we explore the latitudinal extent of the ice line (defined here as the farthest latitude toward the equator where ice is present on a planet's surface), and thus what fraction of the planet is ice-covered, as a function of incident stellar and surface albedo spectrum. Using our radiative transfer model with spectrally resolved absorption coefficients for CO_2, we determine the atmospheric CO_2 concentration necessary to mask surface ice-albedo feedback effects entirely. The manner in which radiative transfer through atmospheric gases is treated can affect our EBM results, and Earth's temperature and ice cover extent have been shown to be greatly influenced by variations in solar radiation (Budyko, 1969). To address these effects, we run a 3-D atmospheric GCM coupled to a motionless 50 m depth "mixed-layer" ocean with a thermodynamic sea ice model. There is no land; hence we refer to it as an aqua planet. We vary the SED of the instellation to investigate the climate of a hypothetical planet of a host M-dwarf star and compare it to the climate of an aqua planet orbiting the Sun, a G-dwarf star, as well as an F-dwarf star, which emits a greater fraction of visible and near-UV radiation. We also describe how changes to the surface albedo parameterization in the GCM affect the climate of an M-dwarf planet. We discuss implications of the results of our climate model simulations for M-dwarf habitability, given the effect of host star SED on climate sensitivity.

2.1. Spectral Mapping Atmospheric Radiative Transfer model

The Spectral Mapping Atmospheric Radiative Transfer model (SMART) is a 1-D, multistream, multilevel, line-by-line, multiple-scattering radiative transfer model developed by David Crisp (Meadows and Crisp, 1996; Crisp, 1997). It is used to generate high-resolution synthetic spectra of planetary atmospheres and surfaces. Recent upgrades and modifications have been made to SMART, including the implementation of Jacobians to support climate modeling. The current version of SMART has been used most recently by Robinson *et al.* (2011) to model Earth. We have used SMART with updated gas absorption line profiles as described in Section 2.4.3. The model uses data on the stellar spectrum, planetary atmospheric composition and temperature, and surface and cloud properties as inputs, and computes wavelength-dependent radiative intensity and flux profiles for both reflected and emitted light. From the computed specific fluxes, we calculate bolometric upwelling and downwelling stellar flux profiles, which we then use to generate the total broadband planetary albedo given the input stellar and surface albedo spectrum.

2.2. Energy balance model

Energy balance climate models (EBMs) simulate the climate from an equation of energy balance of the planet. We used a seasonally varying, 1-D EBM adapted from North and Coakley (1979). The energy balance at each latitude is the sum of absorbed shortwave radiation, outgoing longwave radiation, and the convergence of horizontal heat transport equated with the heat tendency of the vertical column.

We began by coding up the North and Coakley model (1979) ourselves and verified that it reproduced the results of their paper. We then modified it as follows: Heat transport is computed from diffusion of temperature with a latitudinally varying diffusion coefficient, which enhances tropical relative to subtropical heat transport, thus smoothing temperature variations in the tropics and leading to consistency with thermal wind observations (Lindzen and Farrell, 1977). We used idealized land and prescribed time-independent orbital parameters. The instellation is spectrally integrated and varies with latitude and time of year. We also varied the albedo of land, ocean, and below-freezing surfaces, depending on the SED of the instellation. The planetary albedos calculated by SMART with different stellar spectra; an Earth-like atmosphere; and surface albedo files for land, ocean, and

ice of varying grain size are input as broadband albedos over land and ocean in the EBM. This allows the EBM to incorporate to first order the effect of varying SED on the energy balance of the planet. This EBM configuration assumes a rapidly rotating planet like Earth. More work therefore remains to be done to examine alternate spin states such as synchronous rotation, which is expected to prevail in the habitable zones of M-dwarf stars.

There is no explicit ice model; instead the ocean temperature is allowed to be below freezing, which then causes the albedo to increase. We acknowledge that neglecting the energy- and time-dependent dynamics of melting ice will affect the seasonal cycle; therefore we use the EBM primarily to determine the annual mean temperature behavior and defer to the results of our GCM simulations regarding the behavior of the ice margin.

The dependence of outgoing longwave radiation on temperature is linearly parameterized based on the general effect of CO_2 and water vapor on atmospheric radiative transfer as a function of planetary surface temperature. Each latitude has a land and ocean fraction specified to be uniform at 0.01 and 0.99, respectively, to approximate an aqua planet. We evaluated how the ice line latitude changed as a function of modern stellar flux, given the broadband planetary albedos over land, ocean, and ice-covered areas that were calculated by SMART with different stellar spectra as input.

2.3. General circulation model

We used version 4.0 of the Community Climate System Model (CCSM), a fully coupled, global climate model developed to simulate past, present, and future climate states on Earth (Gent *et al.*, 2011). We ran CCSM4 with a 50 m deep, slab ocean (see *e.g.*, Bitz *et al.*, 2012). The slab ocean model normally has ocean heat flux convergence (often called a *q*-flux) input. We set this flux to zero, as done in experiments by Poulsen *et al.* (2001), though we acknowledge that this allows for a snowball transition at a higher instellation than if ocean dynamic heat flux, which tends to buffer against a snowball state, were incorporated (Poulsen *et al.*, 2001; Pierrehumbert *et al.*, 2011). The ocean is treated as static but fully mixed with depth. Simulations that include a fully dynamic ocean, though more realistic, can take thousands of model years to equilibrate for a given radiative forcing and as such are too computationally expensive to allow for the exploration of a wide parameter space as we do here.

The sea ice component is the Los Alamos sea ice model CICE version 4 (Hunke and Lipscomb, 2008), except we have made the ice thermodynamic only (no sea-ice dynamics, which may affect the snowball transition, Abbot *et al.*, 2011) and have reverted back to the sea-ice albedo parameterization from CCSM3. The latter change was made because the newer Delta-Eddington, multiple scattering albedo parameterization is much more difficult to control. In the CCSM3 albedo parameterization, the surface albedo is divided into two bands, visible ($\lambda \leq 0.7\,\mu$m) and near IR ($\lambda > 0.7\,\mu$m). Default near-IR and visible wavelength band albedos are 0.3 and 0.67 for cold bare ice and 0.68 and 0.8 for cold dry snow. The albedos decrease modestly as the surface approaches the melting temperature to mimic the effect of melt ponds. The CCSM3 cold bare ice albedo is approximately halfway between the two end-members for blue marine ice and snow in Fig. 1, while the CCSM3 cold dry snow albedo is between the brightest end-member and three-quarters of the way toward the brightest end-member in Fig. 1. We used the default near-IR and visible-band albedos for all simulations except the surface sensitivity tests described in Section 4.2.4. However, near-IR and visible-band ice albedos calculated by using our ice and snow spectra and weighted by the M-dwarf SED are higher than the default values by 3.3% and 1.5%, respectively, higher by 21% for the visible-band snow albedo, and lower by 23% for the near-IR snow albedo. An implicit error therefore must exist within this range as a result of using the default GCM two-band model and may affect the exact values of temperature and ice extent we calculated for different SEDs. But as the spectral dependence of ice and snow albedo is still captured in the two-band model, the general trends shown here are expected to be robust.

The Community Atmosphere Model version 4 (CAM4.0) divides the incident shortwave (stellar) radiation into 12 wavelength bands, given in Table 1. The percentage of the total flux from the star is specified in these wavelength bands, with a significantly higher percentage of total stellar flux at longer wavelengths (94.6% for M-dwarf star AD Leo, vs. 52.8% for the Sun, and 40.7% for F-dwarf star HD128167 in waveband 10). As AD Leo emits non-negligible amounts of radiation at wavelengths shortward of $0.2\,\mu$m and longward of $5.0\,\mu$m, the percentages of flux in these regions were folded into the shortest (Band 1) and longest (Band 10) wavebands, respectively, to include the full stellar spectrum.

We assumed an Earth-like atmospheric composition for CO_2, H_2O, and O_2. The ozone profile was set to zero, as we were concerned primarily with surface temperature as a measure of planetary habitability and have found the presence of ozone to have a negligible effect on the surface temperature of M- and G-dwarf planets. F-dwarf planets may exhibit colder surface temperatures and greater ice extent with ozone in their atmospheres than without, possibly as a result of greater stratospheric heating in F-dwarf planet atmospheres (Segura *et al.*, 2003), which prevents more shortwave radiation from reaching the surface.

We ran the model on four Intel Xeon hexa-core chips at 2.27 GHz, giving $\sim$11 simulation years per wall-clock day. For each GCM simulation, the model was run for 37 years to equilibrate to the modern Earth climate at present solar instellation. We then ran our simulations for 40 years after that, with varying percentages of instellation with the SED from either the Sun (a G-dwarf star), an M-dwarf star, or an F-dwarf star.

2.4. Model inputs

2.4.1. Stellar spectra. Earlier GCM simulations explored the albedo effects of surface water ice on the climate of M-dwarf planets by using a blackbody distribution to approximate incoming stellar radiation (Pierrehumbert, 2011). Here, we used composite SEDs derived from observations and models of main-sequence (core hydrogen-burning) stars of different spectral types to calculate broadband planetary albedos for a planet covered in specific surface types. We used F2V star HD128167, K2V star HD22049 (Segura *et al.*, 2003), M3V star AD Leo[1] (Reid *et al.*, 1995; Segura *et al.*, 2005), and

[1]http://vpl.astro.washington.edu/spectra/stellar/mstar.htm.

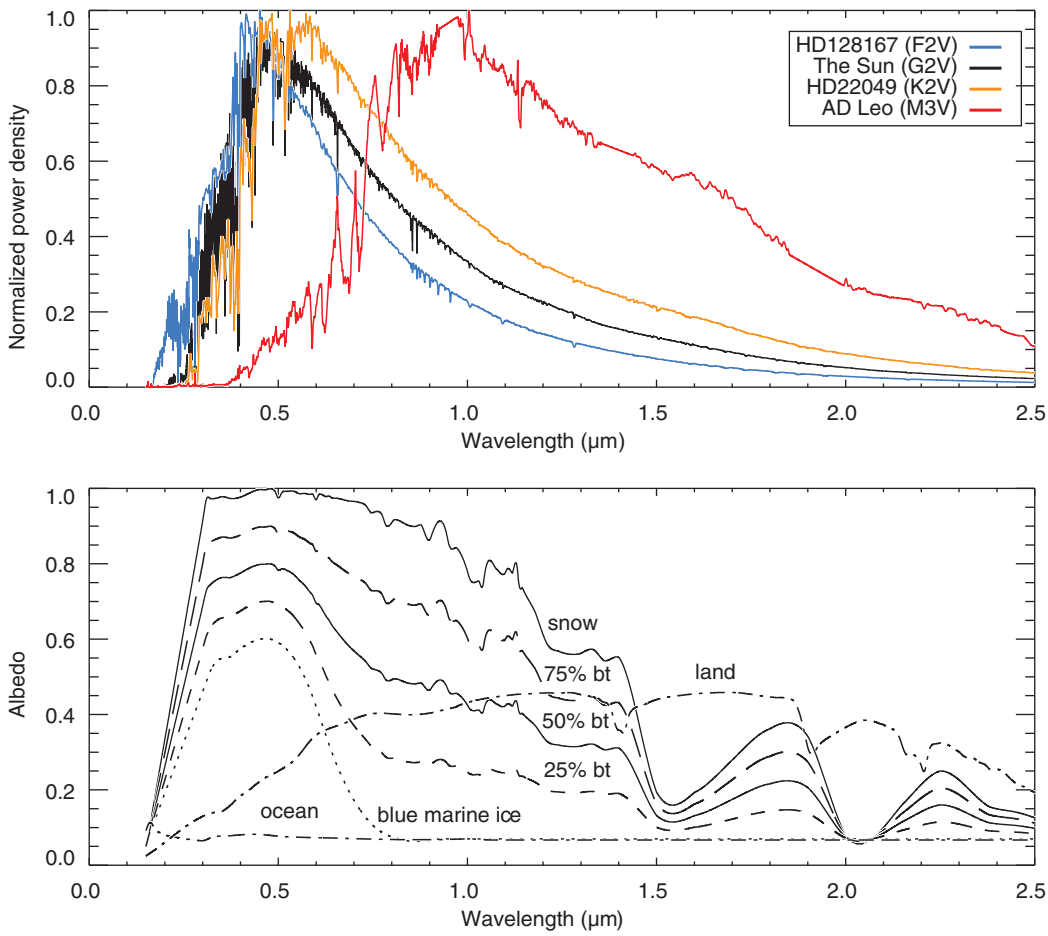

FIG. 1. Top: the SEDs for F-, G-, K-, and M-dwarf stars, normalized by the peak flux. Bottom: the spectral distribution of fine-grained snow, blue marine ice, and 25%, 50%, and 75% mixtures of the two end-members. Ocean and land spectral distributions used in the radiative transfer and energy balance models are also plotted.

the solar spectrum obtained from Chance and Kurucz (2010). All SEDs are shown normalized by their peak flux in Fig. 1. For our SMART runs, all stellar spectra were adjusted so as to integrate to top-of-atmosphere solar constant values of between 1360 and $\sim$1380 W/m^2. For our GCM runs, the value of the solar constant was set to 1360 W/m^2 for all SEDs. This is equivalent to placing our model planets at Earth's equivalent distance from their host stars. The zenith angle varies according to the diurnal cycle in the GCM, and in our SMART runs it was fixed at an average illumination value of 60°.

Table 1. CAM4.0 Spectral Wavelength Bands Specifying Shortwave (Stellar) Incoming Flux into the Atmosphere, and the Percentage of Flux within Each Waveband for the Sun, M-Dwarf Star AD Leo, and F-Dwarf Star HD128167

Band	λ_{min}	λ_{max}	*Sun % flux*	*AD Leo % flux*	*HD128167 % flux*
1	0.200	0.245	0.124	0.025	3.291
2	0.245	0.265	0.130	0.009	0.717
3	0.265	0.275	0.177	0.0029	0.597
4	0.275	0.285	0.167	0.008	0.528
5	0.285	0.295	0.349	0.003	0.763
6	0.295	0.305	0.399	0.004	0.917
7	0.305	0.350	2.805	0.029	4.620
8	0.350	0.640	36.00	3.390	43.12
9	0.640	0.700	6.643	1.895	6.220
10	0.700	5.000	52.79	94.64	40.68
11	2.630	2.860	0.613	1.783	0.393
12	4.160	4.550	0.175	0.749	0.114

2.4.2. Surface albedos. Previous EBMs have employed a broadband frozen surface albedo of 0.6 for M-dwarf star illumination (Pierrehumbert, 2011). Here, we present a more comprehensive look at the effect of incoming stellar radiation on the broadband frozen surface albedo, using high-resolution, wavelength-dependent albedo spectra for multiple water-ice types. We used spectra of albedo as a function of wavelength for fine-grained snow (Grenfell *et al.*, 1994) and for blue marine ice (Warren *et al.*, 2002). Bubbles in glacier ice result from air trapped in snow as it is compressed under the weight of overlying snow. The blue marine ice was not glacier ice; it resulted instead from freezing of liquid water. It contained few bubbles but numerous cracks, which were responsible for the albedo. The cracks are caused by thermal stresses, so they would be present (and contributing to the albedo) even on a planet with no atmosphere (Stephen Warren, private communication). Since these two ice types constitute end-members in terms of ice grain size and albedo at Earth-like surface temperatures and pressures, and ice

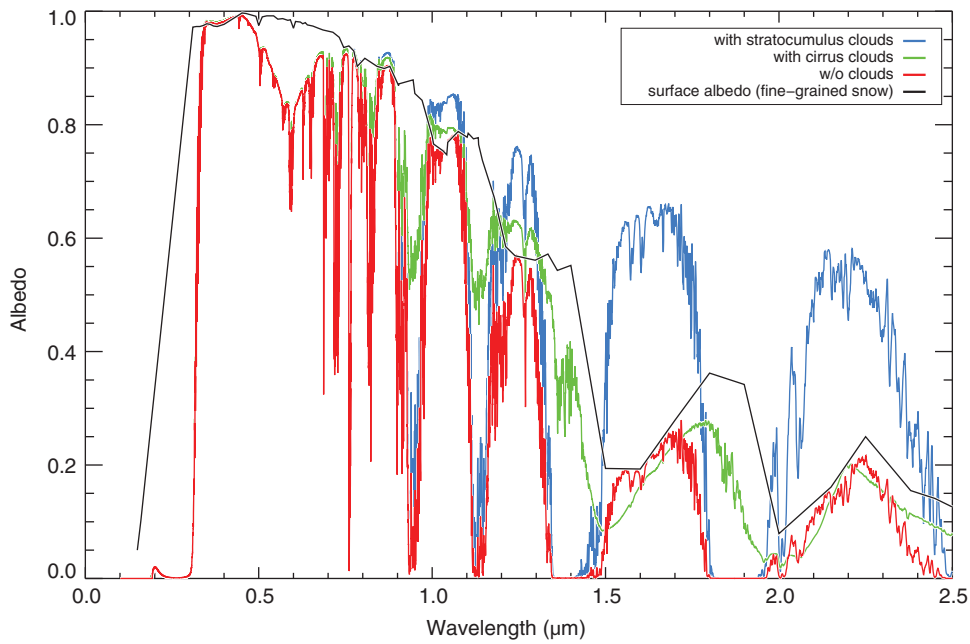

FIG. 2. Wavelength-dependent reflectivity of a planet with an Earth-like atmosphere, an underlying snow surface, clear sky conditions (red), 100% cirrus cloud cover (green), and 100% stratocumulus cloud cover (blue), calculated with SMART. The empirical spectrum for fine-grained snow (from Fig. 1) is plotted here (black) for reference.

may exist between these two states, wavelength-dependent albedo spectra were modeled at 25%, 50%, and 75% mixtures of blue ice and snow (Fig. 1). Albedos for $\lambda < 0.31\,\mu$m were decreased linearly from their values at 0.31 μm down to 0.05 at 0.15 μm for all ice and snow types.

As clouds also exhibit a wavelength-dependent reflectivity, in some cases reaching higher albedos than snow surfaces at longer wavelengths, we plotted the contribution of two major cloud types to Earth's overall reflectivity (Fig. 2) and included them in our model validation in Section 3. Clouds, particularly low stratocumulus clouds, have the largest contribution to Earth's reflectivity at the longest wavelengths of the shortwave spectrum (*i.e.,* 1.5–2.5 μm), where the reflectivity of snow and high cirrus clouds drops significantly. We assume an underlying snow surface in Fig. 2 to highlight the contrast in the wavelength-dependent reflectivity between snow and clouds.

We used an ocean albedo spectrum obtained from Brandt *et al.* (2005). For wavelengths between 0.15 and 0.31 μm, albedos were calculated with the Fresnel equations, with indices of refraction of water from Segelstein (1981). Following Robinson *et al.* (2011), we obtained the spectrum for the clay mineral kaolinite (mixed with trace amounts of smectite and illite) from the United States Geological Survey spectral library[2] for use as the bare land surface in our EBM simulations.

2.4.3. Absorption coefficients. We generated absorption cross sections for relevant gases, using the HITRAN 2008 line list database[3] (Rothman *et al.*, 2009). We then simulated line profiles, using a line-by-line absorption coefficient model (LBLABC, Meadows and Crisp, 1996).

[2]http://speclab.cr.usgs.gov/spectral-lib.html.
[3]http://www.cfa.harvard.edu/hitran.

3. Model Validation

We validated the method of using SMART in combination with an EBM by reproducing Earth's current ice line latitude and global mean surface temperature at its present obliquity, using outgoing IR flux and diffusive heat transport parameterizations as described by North and Coakley (1979). Our maximum and minimum top-of-atmosphere upward fluxes match observations from the Earth Radiation Budget Experiment (Barkstrom and Hall, 1982) to within 6%. We used a temperature-pressure profile for the atmosphere derived using the Intercomparison of Radiation Codes in Climate Models program (ICRCCM). The profile for ICRCCM mid-latitude summer sounding includes atmospheric pressures, temperatures, and mass mixing ratios for seven absorbing gases, and is resolved into 64 vertical layers throughout the atmosphere. We included absorption by H_2O, CO_2, O_3, N_2O, CO, CH_4, and O_2, and Rayleigh scattering. Broadband planetary albedos for the surface types described in Section 2 were generated assuming both clear and cloudy sky conditions. Approximately 64% of Earth is covered in clouds (Warren and Hahn, 2002). Two cloud layers were used—that of low stratocumulus clouds and high cirrus clouds. For the purposes of our model, we assumed 36% clear sky conditions, 40% low stratocumulus clouds, and 24% high cirrus clouds. Average broadband albedos over ocean, land, and regions where the surface temperature falls below −2°C were calculated as described by Zsom *et al.* (2012), with the use of these cloud fractions as well as the combined cloud fraction assuming random overlap between the two cloud layers (Oreopoulos and Khairoutdinov, 2003). An optical depth of 10 was used for both cloud types. A modern land/ocean geographical configuration was used in the EBM. Areas over ocean and land surfaces were assigned broadband albedos of 0.32 and 0.41, respectively. Regions where

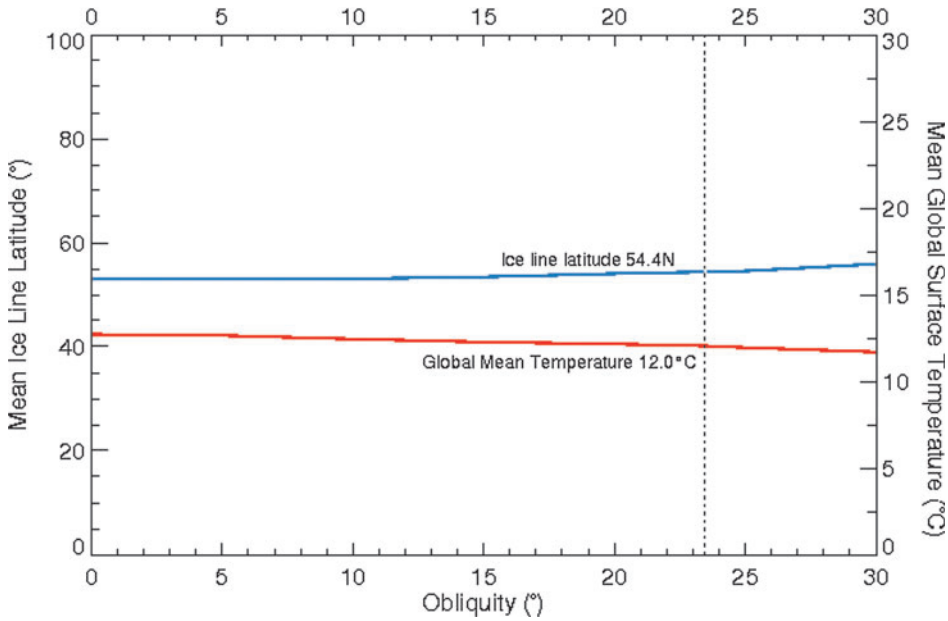

FIG. 3. Mean ice line latitude and global surface temperature as a function of obliquity, calculated using a seasonal EBM. Earth's northern hemisphere ice line latitude and global mean surface temperature at its present obliquity of 23.5° (vertical dashed line) are verified to within six degrees in latitude and 3°C, respectively. Ocean and land surfaces were assigned broadband albedos of 0.32 and 0.41, respectively (including atmosphere, for 36% clear sky, 40% stratocumulus cloud cover, and 24% cirrus cloud cover). Regions where the surface temperature fell below −2°C were assigned a broadband albedo of 0.46, which was calculated by using the same percentages of clear sky and cloud cover, with the spectrum corresponding to the 25% mixture of blue marine ice and fine-grained snow in Fig. 1. Random overlap between the two cloud layers is assumed. Color images available online at www.liebertonline.com/ast

the surface temperature fell below −2°C were assigned a broadband albedo of 0.46, which corresponds to the 25% mixture of blue marine ice and fine-grained snow in Fig. 1. The EBM ice line latitude is 54.4°N, which is within 6° of Earth's northern hemisphere ice line latitude as defined as the southernmost tip of Greenland by Kukla (1979) and Mernild *et al.* (2010). The EBM global mean surface temperature (including zonal mean land and ocean temperatures) is 12°C and within three degrees of the global mean surface temperature of Earth as defined as 15°C by Hartmann (1994). The EBM ice line latitude and global mean surface temperature (Fig. 3) were calculated by using only the surface types in Fig. 1.

We assumed a water vapor concentration equal to a midlatitude average of 1% of the atmosphere at 1-bar surface pressure to calculate broadband planetary albedos used in our model validation. The amount of water vapor decreases rapidly with increasing latitude and can be as much as 10 times lower at the poles (Hartmann, 1994). To test the sensitivity of our calculated albedos to water vapor, we ran SMART with 0.1% water vapor and found our broadband albedos over land, ocean, and below-freezing surface types to increase by no more than 10% for ocean and ice surfaces and 13% for our land spectrum.

4. Results

4.1. SMART+EBM

We used SMART to comprehensively address the radiative transfer that takes place between a planet's ice, ocean, and land surfaces and the incident stellar radiation. Derived broadband planetary albedos used as input to the EBM are therefore unique to the planet-star system, rather than broadly generalized. Here, we first explore the contributions to broadband planetary albedo for different surface types, atmospheric pressures, and stellar SEDs. We then explore climate sensitivity to changes in instellation, surface type, and ice grain particle size for Earth-like planets orbiting stars of different spectral type.

4.1.1. Contributions to broadband planetary albedo. Figure 4 shows broadband planetary albedos that are output from SMART, given various surface types (where broadband, or "Bond" albedo is defined as the ratio of the total amount of flux reflected by the planet, divided by the total flux incident on the planet, integrated over the entire wavelength spectrum).

We were primarily interested in quantifying the effects of surface albedo on planetary climate and used the aqua planet EBM as a test bed for identifying general trends. Broadband planetary albedos decrease monotonically with stellar luminosity, even though all stellar spectra have been adjusted to provide the same integrated flux as that received by Earth around the Sun. This can be explained by the larger fraction of spectral energy emitted at $\lambda > 1.0\,\mu$m for stars with lower luminosities. These broadband planetary albedos incorporate the wavelength-dependent reflectivity of the underlying surface. At these longer wavelengths, ice and snow absorb strongly (Fig. 1), resulting in a lower average surface albedo contribution to the overall planetary albedo.

Since Rayleigh scattering is stronger at shorter wavelengths due to the $1/\lambda^4$ cross-section dependence, it is expected to be more pronounced on an F-dwarf planet than on

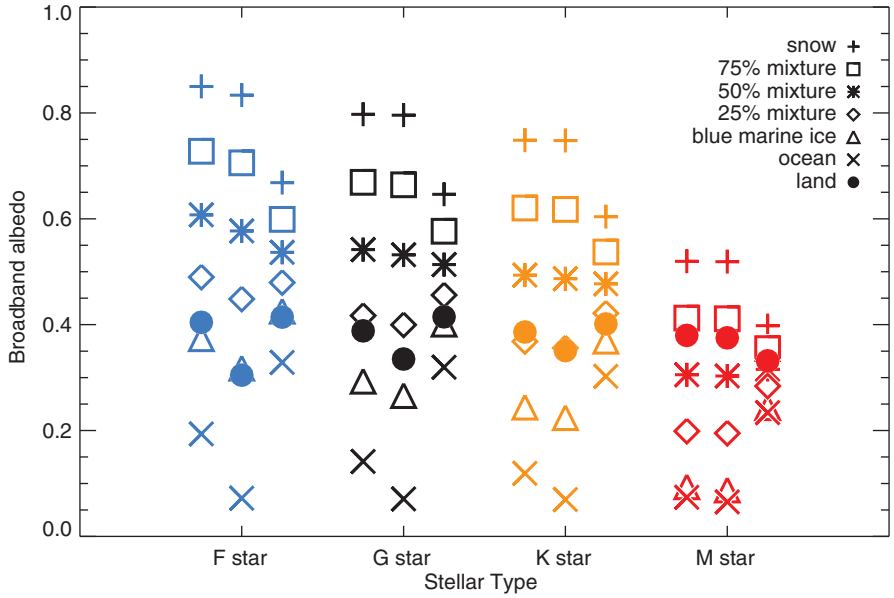

FIG. 4. Broadband planetary albedos calculated with upwelling and direct downwelling stellar flux outputs from SMART for ice, snow, ocean, and land surfaces given the SEDs of F-, G-, K-, and M-dwarf stars. For each star: Left—no atmospheric gas absorption, but Rayleigh scattering is included; middle—no gases or Rayleigh scattering (broadband F-dwarf planetary albedos for ice and snow surfaces are still larger than those for G-, K-, or M-dwarf planets, even after the effects of Rayleigh scattering are removed); right—Rayleigh scattering, gas absorption, and clouds are included. These values are listed in Table 2. Color images available online at www.liebertonline.com/ast

other host star planets and can result in higher broadband planetary albedos (Kasting *et al.*, 1993; Pierrehumbert, 2011; Kopparapu *et al.*, 2013a). To verify the trend stated above, we reduced the atmospheric pressure in additional SMART runs with an F-dwarf spectrum incident on an ocean surface and excluded atmospheric gases. We confirmed that the Rayleigh scattering tail present at $\lambda < 0.7\,\mu$m for atmospheres with 1-bar surface pressure is virtually absent for thin atmospheres of less than 0.1 mbar (Fig. 5). The resulting broadband albedos in the "no Rayleigh scattering" case are plotted in Fig. 4 (middle column). Even with Rayleigh scattering removed, Fig. 4 reveals higher broadband planetary albedos with ice and snow surfaces for the F-dwarf host star and the lowest broadband albedos for the M-dwarf host star. Also plotted are broadband planetary albedos calculated with Rayleigh scattering only (no atmospheric gas absorption, left column) and with both Rayleigh scattering, atmospheric gases, and clouds included (right column). These values for each stellar type are listed in Table 2.

4.1.2. Climate sensitivity for Earth-like planets. Broadband planetary albedos calculated from SMART (with an Earth-like atmospheric composition and distribution of clouds) were used as input to the EBM. Below-freezing surfaces encountered during the EBM runs (where the temperature is less than −2°C) were given broadband planetary albedos for ice and snow of varying grain size calculated from SMART at 1-bar surface pressure. EBM simulations were run with an initial warm start, with an approximate Earth-like zonal mean temperature distribution. The global mean surface temperature and mean latitude of the ice line in the northern hemisphere were calculated at present Earth obliquity (23.5°) as a function of percent of modern solar constant, with 100% of the modern solar

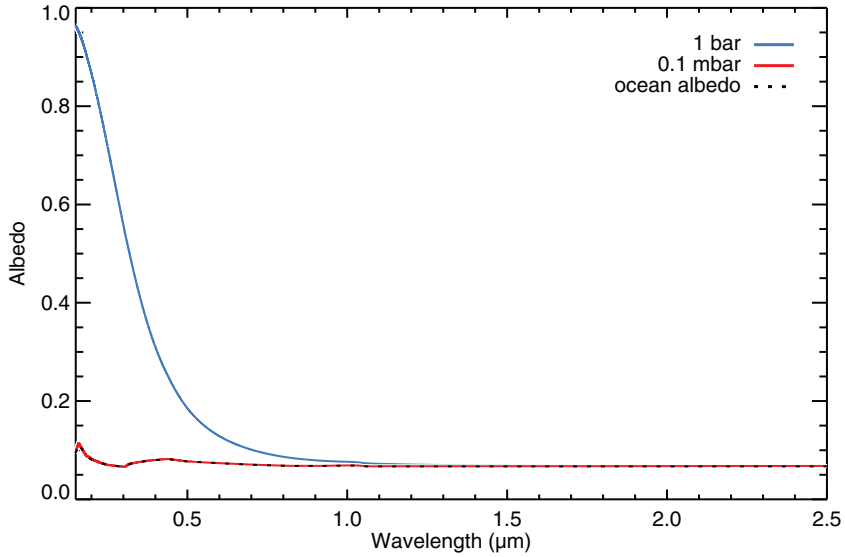

FIG. 5. Top-of-atmosphere upwelling flux divided by the downwelling stellar flux (which is a measure of the planetary albedo) as a function of wavelength for an ocean-covered planet with a surface pressure of 1 bar and 0.1 mbar orbiting an F-dwarf star at an equivalent flux distance to Earth around the Sun, calculated with SMART. No atmospheric gas absorption is included here. The rise in top-of-atmosphere flux (and therefore planetary albedo) evident in the 1-bar atmosphere case at $\lambda < 0.7\,\mu$m is due to Rayleigh scattering. At 0.1 mbar, the Rayleigh scattering tail is absent and matches the empirical albedo spectrum of the ocean surface from Fig. 1 (dotted black). Color images available online at www.liebertonline.com/ast

Table 2. Broadband Planetary Albedos Calculated with Upwelling and Direct Downwelling Stellar Flux Outputs from SMART for Fine-Grained Snow, Large-Grained Blue Marine Ice, Ice of Intermediate Density between the Two End-Members, Ocean, and Land Surfaces, Given the SEDs of F-Dwarf Star HD128167, the Sun (a G-Dwarf Star), K-Dwarf Star HD22049, and M-Dwarf AD Leo

Stellar type	*Surface*	*No gases or clouds Rayleigh scattering on*	*No gases or clouds Rayleigh scattering off*	*Earth-like gases, clouds Rayleigh scattering on*
F dwarf	snow	0.84988	0.83361	0.66833
	75%	0.72756	0.70568	0.59884
	50%	0.60744	0.57704	0.53664
	25%	0.48993	0.44840	0.47961
	blue ice	0.37330	0.31782	0.42542
	ocean	0.19349	0.07221	0.32865
	land	0.40438	0.30470	0.41428
G dwarf	snow	0.79724	0.79577	0.64622
	75%	0.66882	0.66421	0.57636
	50%	0.54191	0.53194	0.51363
	25%	0.41708	0.39966	0.45585
	blue ice	0.29312	0.26603	0.40093
	ocean	0.14155	0.07070	0.31948
	land	0.38829	0.33513	0.41484
K dwarf	snow	0.74842	0.74784	0.60392
	75%	0.62041	0.61768	0.53716
	50%	0.49350	0.48685	0.47708
	25%	0.36822	0.35602	0.42150
	blue ice	0.24418	0.22435	0.36870
	ocean	0.11921	0.06965	0.30235
	land	0.38606	0.35098	0.40133
M dwarf	snow	0.51963	0.51905	0.39800
	75%	0.41245	0.41125	0.35478
	50%	0.30542	0.30308	0.31546
	25%	0.19890	0.19491	0.28406
	blue ice	0.09361	0.08749	0.24317
	ocean	0.07390	0.06518	0.23372
	land	0.37974	0.37516	0.33165

For the planetary albedos that include gases and clouds (right column), average broadband albedos were calculated as described in Zsom *et al.* (2012) assuming 64% cloud cover (Warren and Hahn, 2002), with 40% low stratocumulus clouds and 24% high cirrus clouds. Random overlap between the two cloud layers is assumed (Oreopoulos and Khairoutdinov, 2003).

constant being the present amount of solar instellation, or flux density, on Earth. The results are plotted in Fig. 6 and can be assumed to be similar for the southern hemisphere, given an assumed eccentricity of zero. The slope of each line is a measurement of the climate sensitivity of the planet to changes in instellation. The smaller the grain size of the ice (and therefore the higher the albedo), the farther toward the equator the ice advances. For stars with higher visible and near-UV output, ice-covered planetary states occur with smaller decreases in instellation. Cooler, redder stars allow planets to remain free of global ice cover with larger decreases in instellation. It must be noted that an alternate branch of these results exists with significant ice cover if an initial cold start is assumed, with zonal mean temperatures characteristic of a snowball state. We have not explored those states here.

4.2. GCM simulations

One-dimensional EBMs offer insight into the latitudinally resolved distribution of temperature and ice across a planet. However, they heavily parameterize atmospheric radiative transfer and eddy heat transport. Furthermore, ours only captures the albedo effects of sea ice (not the insulating effect). To test the robustness of the results from our EBM simulations and provide further physical insight into the contribution of atmospheric dynamics to planetary climate, we employed a coupled atmospheric GCM with more complete sea ice physics. Coupled GCMs are crucial to understanding the full planetary response to changes in radiative and surface forcing. This is demonstrated in Fig. 7, where the top-of-atmosphere absorbed shortwave radiation minus outgoing longwave radiation as a function of latitude in an EBM is compared with that in a GCM for a G-dwarf planet receiving 100% of the modern solar constant. When averaged over a few years or more, the net incoming heat flux must be equal to the divergence of heat from each grid cell in order to yield a net surface flux of zero locally and globally in our slab ocean model. The EBM shows a large jump in the net incoming heat flux near the poles, due to the abrupt change in albedo for ice-covered areas in the EBM and the lack of parameterized clouds (beyond our SMART treatment). This large jump causes the ice line to be unstable and collapse to the equator at significantly higher latitudes in the EBM compared to the GCM. A smoother transition in net

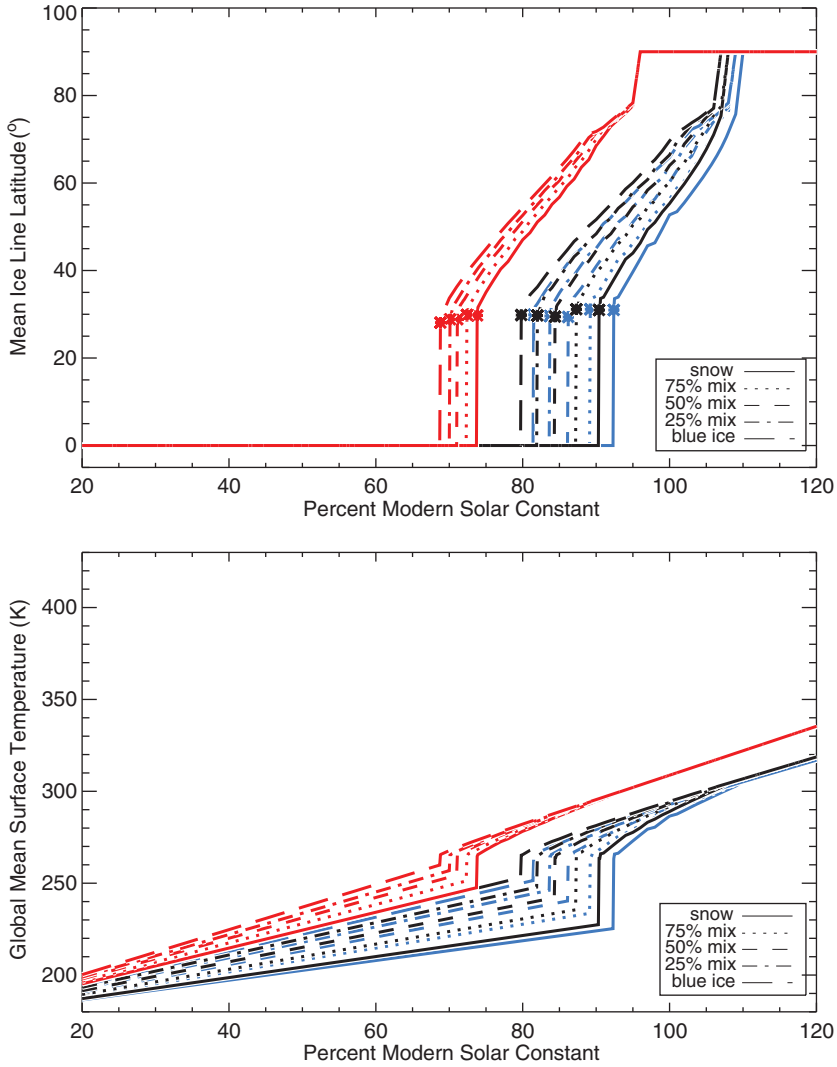

FIG. 6. Mean ice line latitude (top) and global mean surface temperature (bottom) in the northern hemisphere as a function of percent of modern solar constant are calculated by using a seasonal EBM, at present Earth obliquity (23.5°) for aqua planets (land and ocean fraction 0.01 and 0.99, respectively) orbiting F-, G-, and M-dwarf stars at an equivalent flux distance. Below-freezing surfaces encountered during the EBM runs (where the temperature is less than −2°C) were given broadband planetary albedos for ice and snow of varying grain size calculated from SMART at 1-bar surface pressure. EBM simulations were run with an initial warm start, with an approximate Earth-like zonal mean temperature distribution. The results can be assumed to be similar for the southern hemisphere, given an assumed eccentricity of zero. The present atmospheric level of CO_2 was used (F-dwarf planet in blue, G-dwarf planet in black, and M-dwarf planet in red). Asterisks denote the minimum ice line latitude before collapse to the equator and global ice coverage.

incoming heat flux as a function of latitude is visible in the GCM, due to the presence of full-scale atmospheric dynamics, including clouds. The ice line latitude is stable 17–24° farther toward the equator for all simulated aqua planets (Fig. 8) than those calculated in the EBM (Fig. 6), yielding gentler transitions in latitudinal ice extent and global mean surface temperature as a function of percent of modern solar constant in the GCM than is seen in the EBM. As the slopes of the lines in Figs. 6 and 8 are a measure of the climate sensitivity of the planets, the GCM results indicate a lower climate sensitivity to changes in instellation than would be inferred from the EBM results alone.

We begin our analysis of GCM simulations by characterizing how the global climate depends on the stellar constant for an aqua planet orbiting the Sun or an M- or F-dwarf star. Then we describe the climates in greater detail for an aqua planet around the Sun and an M-dwarf star, where we consider runs with similar temperate climates but vastly different SEDs, followed by stellar constants that give similar snowball climates. We explore the role played by atmospheric dynamics in generating similar ice-covered states, given the different stellar SEDs. Finally, we investigate the sensitivity of planetary climate to surface albedo alone.

4.2.1. Climate sensitivity: G-dwarf versus M-dwarf and F-dwarf planets. Figure 8 shows the latitudinal ice extent and annual global mean surface temperature in the northern hemisphere as a function of percent of modern solar constant for a G-dwarf aqua planet with an incident spectrum of the Sun, an M-dwarf aqua planet with the incident spectrum measured for AD Leo, and an F-dwarf aqua planet with the incident spectrum measured for HD128167. As we assumed an eccentricity of zero in our GCM runs, an obliquity of 23°, and no land surface, the temperature and ice behavior are symmetrical in the time-mean about the equator over an annual cycle. A comparison of 3-D simulations of the climate of a planet receiving 90% of the modern solar constant ($1224\,W/m^2$) from an M dwarf with one receiving 90% flux from the Sun yields significant differences in the resulting climate states. The planet receiving the Sun's SED is completely ice-covered, with a global mean surface temperature of 215 K, while the planet receiving the M-dwarf star's SED is 72 degrees hotter (at ∼288 K, see Fig. 8). This is largely due to the increased absorption of the predominantly near-IR radiation emitted by M-dwarf stars by atmospheric CO_2 and water vapor. This results in a much larger greenhouse effect that keeps the M-dwarf planet's surface warmer than the G-

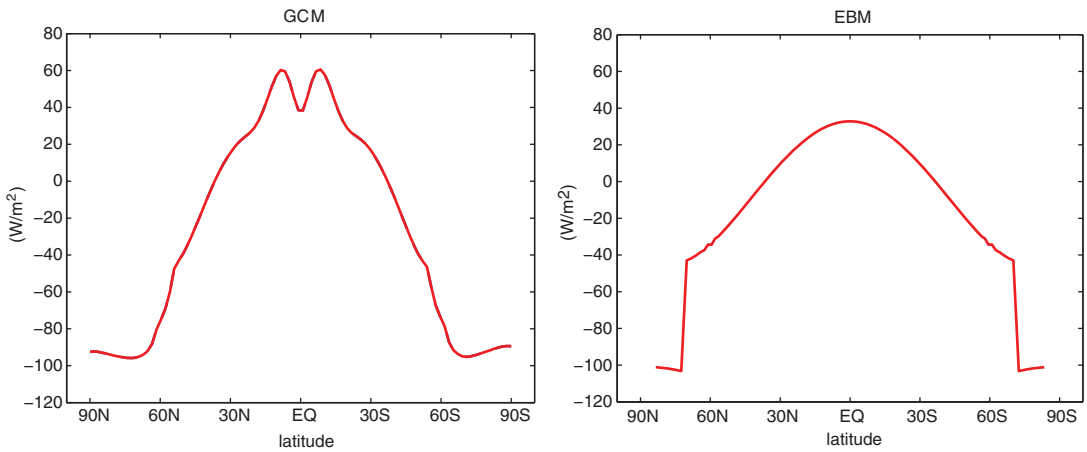

FIG. 7. Top-of-atmosphere absorbed shortwave radiation minus outgoing longwave radiation as a function of latitude, calculated in the GCM (left) and the EBM (right) for a G-dwarf planet receiving 100% of the modern solar constant. When averaged over a few years or more, the net incoming heat flux must be equal to the divergence of heat from each grid cell in order to yield a net surface flux of zero locally and globally in our slab ocean model. The EBM shows a large jump in the net incoming heat flux near the poles, due to the abrupt change in albedo for ice-covered areas in the EBM, and lack of parameterized clouds (beyond our SMART treatment). A smoother transition in net incoming heat flux as a function of latitude is visible in the GCM, due to the presence of full-scale atmospheric dynamics, including clouds.

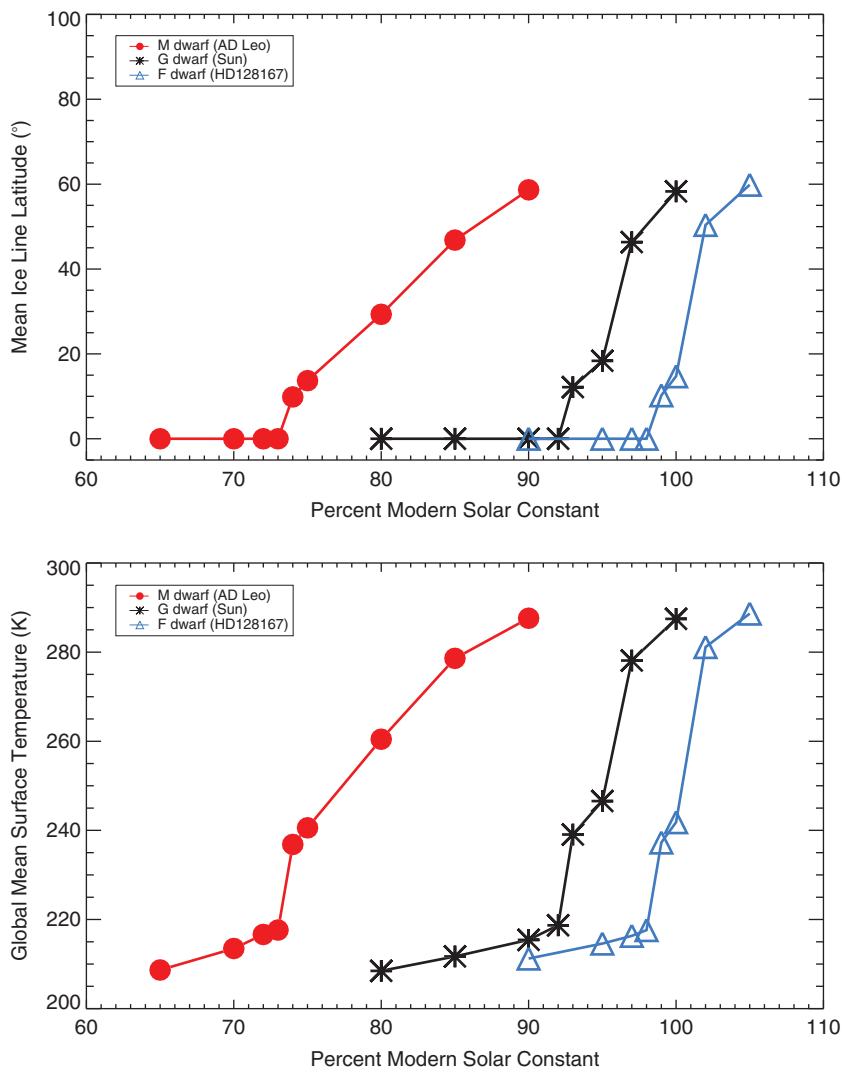

FIG. 8. Mean ice line latitude (top) and global mean surface temperature (bottom) as a function of percent of modern solar constant after a 40-year GCM run for an aqua planet orbiting the Sun (asterisks), M-dwarf star AD Leo (circles), and F-dwarf star HD128167 (triangles) at equivalent flux distances. The slope of each line is a measurement of the climate sensitivity of the planet to changes in stellar flux. The shallower slope of the M-dwarf planet indicates a smaller change in surface temperature and ice extent for a given change in instellation than on the planets orbiting stars with greater visible and near-UV output.

dwarf planet (Kasting *et al.*, 1993; Selsis *et al.*, 2007). The M-dwarf planet's global mean surface temperature and ice line latitude (58.7°) are in better agreement with the global mean surface temperature and latitudinal ice extent on a G-dwarf planet receiving 100% of the modern solar constant ($\sim$1360 W/m^2), which are 287 K and 58.3°, respectively. One-dimensional radiative-convective calculations by Kasting *et al.* (1993) yielded comparable stratospheric water-vapor mixing ratios and planetary surface temperatures between G- and M-dwarf planets when the M-dwarf planet received 10% less flux from its star compared to the G-dwarf planet, though the emission from the stars in their simulations was approximated by blackbody radiation (Kasting *et al.*, 1993).

With the CO_2 held fixed at 400 ppm, we started with simulations that would result in similar surface climate conditions on F-, G-, and M-dwarf aqua planets. On an F-dwarf planet, this required that the instellation be increased to 105% of the modern solar constant in order to yield a comparable global mean surface temperature and ice line latitude (289 K and 59.8°, respectively) to the G-dwarf planet receiving 100% of the modern solar constant (287 K and 58.3°). On an M-dwarf planet, an instellation equal to 90% of the modern solar constant is all that is required to yield a comparable global mean surface temperature and ice line latitude (288 K and 58.7°) to the G-dwarf planet receiving 100% of the modern solar constant.

On an F-dwarf planet receiving 100% of the modern solar constant, the ice line latitude is $\sim$15°. This is 43° farther toward the equator than the ice line latitude on a G-dwarf planet receiving equivalent instellation. A snowball state (where the ice covers the entire hemisphere, with a mean ice line latitude of 0°) then occurs on the F-dwarf planet with a 2% further reduction in instellation, to 98% of the modern solar constant (Fig. 8). An 8% reduction in instellation from the Sun is required to plunge the G-dwarf planet into global ice cover, at 92% of the modern solar constant. Ice on our M-dwarf planet does not extend all the way to the equator until the instellation has been reduced by an additional 19% compared to the G-dwarf planet, equivalent to 73% of the modern solar constant ($\sim$979 W/m^2). In Fig. 8, the slope of the curve with decreasing stellar flux for the M-dwarf planet is much shallower than those for the G- and F-dwarf planets, indicating a much lower change in surface temperature and ice extent for a given change in stellar flux on the M-dwarf planet.

As stated earlier, in our GCM simulations the ice line extends farther before unstable collapse to the equator than the critical latitude of 25–30° often required by diffusive EBMs. EBMs that transport less heat across the ice line, as well as fully coupled atmosphere-ocean GCMs, have been found to permit stable ice lines at lower latitudes (Poulsen *et al.*, 2001; Pollard and Kasting, 2005). Cloud cover has also been shown to serve as a negative feedback on the latitudinal extent of tropical sea ice, as it contributes little additional reflectivity when located over high-albedo surfaces but still adds to the greenhouse effect (Poulsen *et al.*, 2001). Increased cloud cover may therefore contribute to stabilizing the ice edge in GCMs. And stable climate states with extremely low-latitude (but not equatorial) ice coverage on planets orbiting the Sun have been generated with climate models as a result of large albedo differences between bare sea ice and snow-covered ice (Abbot *et al.*, 2011). The fact that the ice line extends farthest toward the equator without collapsing to a snowball state on the M-dwarf planet than on the G- or F-dwarf planets is likely a consequence of the lower-albedo ice on the M-dwarf planet's surface. Indeed, the average albedo of the (mostly ice-covered) M-dwarf planet receiving 74% of the modern solar constant (the lowest amount of instellation received by the planet in our simulations without becoming completely ice-covered) is 0.51, while the G- and F-dwarf planets with slightly less ice coverage (receiving 93% and 99% of the modern solar constant, respectively), have mean albedos of 0.55 and 0.58.

4.2.2. 90% M-dwarf versus 100% G-dwarf: the climatic effect of stellar host SED. The global mean surface temperature of the M-dwarf planet receiving 90% of the modern solar constant is quite similar to that of a G-dwarf planet receiving the full modern solar constant (100%), differing by less than 1 K. The latitudinal surface temperature profile is also strikingly similar (Fig. 9), although the M-dwarf planet exhibits warmer temperatures at the poles. To understand how the M-dwarf planet is compensating for the decreased instellation, we first take a closer look at the atmospheres of the two planets.

While the surface temperature profiles of both planets appear relatively similar at subpolar latitudes, there is about $\sim$10% less precipitation on the M-dwarf planet everywhere except at the poles (Fig. 10). Precipitation is lower on the M-dwarf planet because there is less shortwave radiation reaching the surface to drive evaporation.

The shift toward longer wavelengths in the M-dwarf star SED gives rise to a greater amount of shortwave heating due to absorption in the M-dwarf planet's atmosphere than on the G-dwarf planet, particularly in the tropics (Fig. 11a–c). The plot of zonal mean vertical temperature follows a similar pattern, with higher temperatures throughout most of the atmospheric column in the tropics and at the poles, which

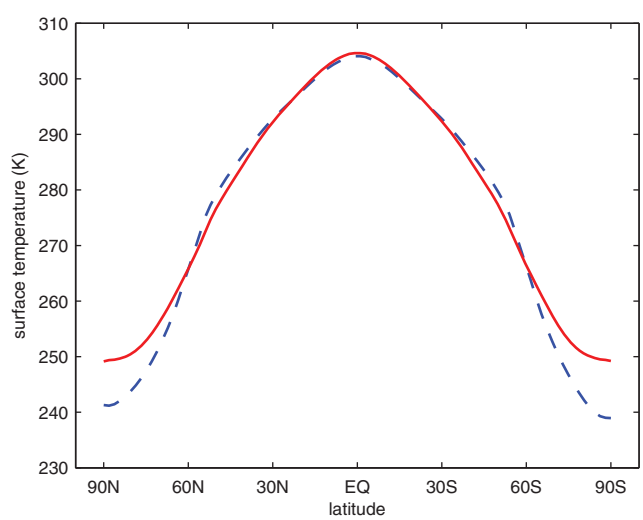

FIG. 9. Surface temperature on an aqua planet receiving 90% of the modern solar constant from an M-dwarf star (red) compared with an aqua planet receiving 100% of the modern solar constant from the Sun, a G-dwarf star (blue dashed), after a 40-year GCM run. Color images available online at www.liebertonline.com/ast

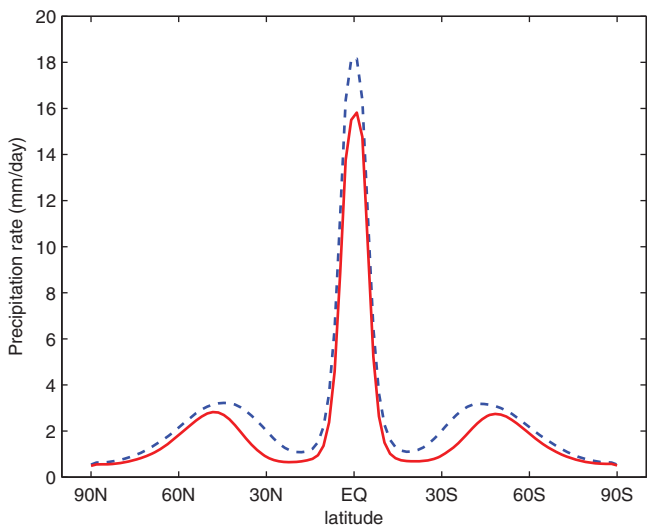

FIG. 10. Precipitation rate on an aqua planet receiving 90% of the modern solar constant from an M-dwarf star (red) compared with an aqua planet receiving 100% of the modern solar constant from the Sun (blue dashed), after a 40-year GCM run. Color images available online at www.liebertonline.com/ast

indicates a smaller lapse rate over most of the troposphere on the M-dwarf planet than on the G-dwarf planet (Fig. 11d–f). The weaker Hadley circulation on the M-dwarf planet (Fig. 12) contributes to the greater tropospheric temperatures. However, near the surface, the difference in atmospheric temperature between the two planets is minimal. The stability of the atmospheres is therefore similar near the surface, but the M-dwarf planet appears more stable over the free troposphere, resulting in less cloudiness at most heights (Fig. 13), less precipitation, and more shortwave radiation absorbed by the planet. The more absorbing ice and snow on the M-dwarf planet (Fig. 14) allows the polar regions of the M-dwarf planet to be slightly warmer than the G-dwarf planet, with a similar ice line latitude despite the greatly reduced instellation.

4.2.3. 73% M-dwarf versus 92% G-dwarf: a comparison of snowball planets. GCM simulations of an aqua planet receiving 73% of the modern solar constant from an M-dwarf star and an aqua planet receiving 92% of the modern solar constant from the Sun result in similar surface conditions, with ice extending all the way to the equator on both planets. A comparison of zonal mean vertical temperature on the two snowball planets shows higher temperatures in the upper troposphere of the M-dwarf planet (likely a consequence of greater shortwave heating due to absorption in the M-dwarf planet's atmosphere, as described in the previous section) but minimal difference in atmospheric temperature between the two planets near the surface (Fig. 15). Surface shortwave downwelling flux is the amount of flux from the host star that passes through the atmosphere and reaches the surface of the planet. Since the G-dwarf planet receives 19% more radiation from its star than the M-dwarf planet, much more shortwave radiation reaches the surface of the G-dwarf planet (Fig. 16a). However, the G-dwarf planet's surface is more reflective, due to the greater percentage of visible radiation (as discussed in Section 1) incident on the G-dwarf planet (Fig. 16b). As a result, the G-dwarf planet cannot absorb enough shortwave radiation to avoid full ice cover. Higher absorption of the shortwave spectrum incident on the surface of the M-dwarf planet compensates for the reduced instellation, resulting in similar amounts of shortwave radiation absorbed on the surfaces of both planets (Fig. 16c) and similar global mean surface temperatures of $\sim$218 K (Fig. 16d). Indeed, of the total shortwave flux that reaches the surface of the M-dwarf planet, $\sim$44% is absorbed by the surface at the equator, and $\sim$30% is absorbed at the poles, compared with $\sim$35% absorbed at the equator and $\sim$25% at the poles on the G-dwarf planet. The three peaks in surface-absorbed shortwave in the tropics and subtropics on the G-dwarf planet in Fig. 16c result from local minima in the surface albedo (Fig. 16b) where evaporation exceeds precipitation and hence snow depths are locally smaller.

4.2.4. Testing climate sensitivity to surface albedo. Since the atmosphere of the M-dwarf planet absorbs such a large amount of the shortwave radiation, lowering the overall planetary albedo, it was important to verify whether the spectral dependence of surface ice albedo had any discernible effect on a planet's climate at Earth-like atmospheric CO_2 levels. By lowering the IR and visible-band cold ice and snow albedos for an M-dwarf planet to 0.2, thereby significantly reducing the difference between ice and ocean on the planet's surface, we were able to examine the effect on climate sensitivity of surface ice and snow albedo interacting with the host star SED. Ice and snow albedos were lowered on M-dwarf planets receiving 75% and 85% of the modern solar constant, and the results were compared with model runs with the default albedo parameterization (see Section 2.3) for planets receiving equivalent instellation. The results are plotted in Fig. 17.

The result for both M-dwarf planets is a warmer climate and less ice than with the default albedo parameterization. The difference in climates is larger between the M-dwarf planets receiving 75% instellation than between the M-dwarf planets receiving 85% instellation, as indicated by the black vertical lines in Fig. 17. This is because there is a higher surface coverage of ice on the M-dwarf planet receiving lower instellation, resulting in a larger impact on the planet's climate when the ice and snow albedos are lowered, including larger increases in temperature, cloudiness, and precipitation. As a result, the M-dwarf planet's slope of the temperature and ice extent as a function of instellation is much shallower than that of the M-dwarf planet runs with the default albedo parameterization. This shallower slope implies a smaller change in surface temperature and ice extent for a given change in instellation, indicating that a planet's climate is sensitive to surface ice and snow albedo, even with an Earth-like atmospheric concentration of greenhouse gases.

4.3. High-CO_2 atmosphere: the outer edge of the habitable zone

Atmospheric CO_2 concentrations are expected to increase farther out in the habitable zone, where decreased silicate weathering would lead to CO_2 building up in the atmosphere (Walker *et al.*, 1981). CO_2 content at the OHZ would therefore be high and could reach levels of over 2 bar before

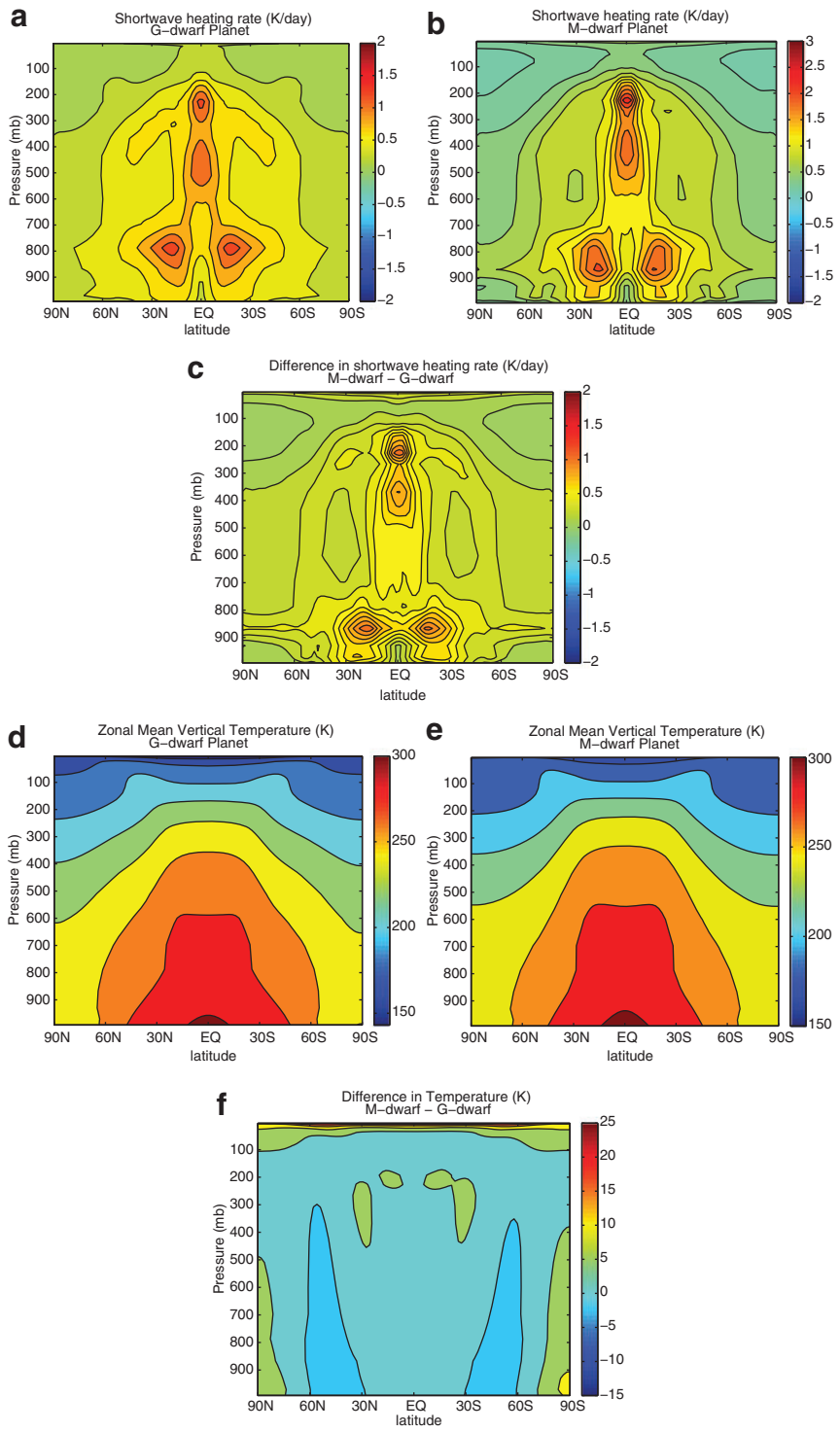

FIG. 11. GCM comparison of an M-dwarf aqua planet receiving 90% of the modern solar constant compared with an aqua planet receiving 100% of the modern solar constant from the Sun, a G-dwarf star. (**a**) Shortwave heating in the atmosphere of the G-dwarf planet; (**b**) shortwave heating in the atmosphere of the M-dwarf planet; (**c**) increase in shortwave heating in the atmosphere of the M-dwarf planet, calculated by taking the difference between the M-dwarf planet's shortwave heating profile and the G-dwarf planet's shortwave heating profile; (**d**) zonal mean temperature in the atmosphere of the G-dwarf aqua planet; (**e**) zonal mean temperature in the atmosphere of the M-dwarf aqua planet; (**f**) increase in zonal mean temperature in the atmosphere of the M-dwarf aqua planet, calculated by taking the difference between the M-dwarf planet's atmospheric temperature profile and the G-dwarf planet's atmospheric temperature profile.

reaching the maximum CO_2 greenhouse limit (Pierrehumbert, 2010). Given that CO_2 has a number of absorption bands in the near IR, where M-dwarf stars emit strongly and snow albedo drops significantly, we ran sensitivity tests to quantify the effect of CO_2 on the suppression of the cooling effect of ice-albedo feedback for M-dwarf planets. Runs were completed with SMART and included a case for a pure nitrogen atmosphere with little to no near-IR gas absorption and cases for atmospheres consisting of 10% CO_2 and 90% N_2; 50%/50% CO_2/N_2; and pure CO_2 atmospheres at 2-, 3-, 10-, 12-, 14-, and 15-bar surface pressures. For these sensitivity tests, no clouds were incorporated. For atmospheric pressures greater than 1 bar, the vertical pressure profile was multiplied by the desired integer scaling factor, and the molecular weight of the atmosphere was adjusted accordingly. We did two runs at each atmospheric concentration: one with the actual fine-grained snow albedo spectrum from Grenfell *et al.* (1994), which drops to low values in the near IR, and one where the Grenfell snow spectrum was altered to exhibit artificially high albedo values of 0.6 at wavelengths

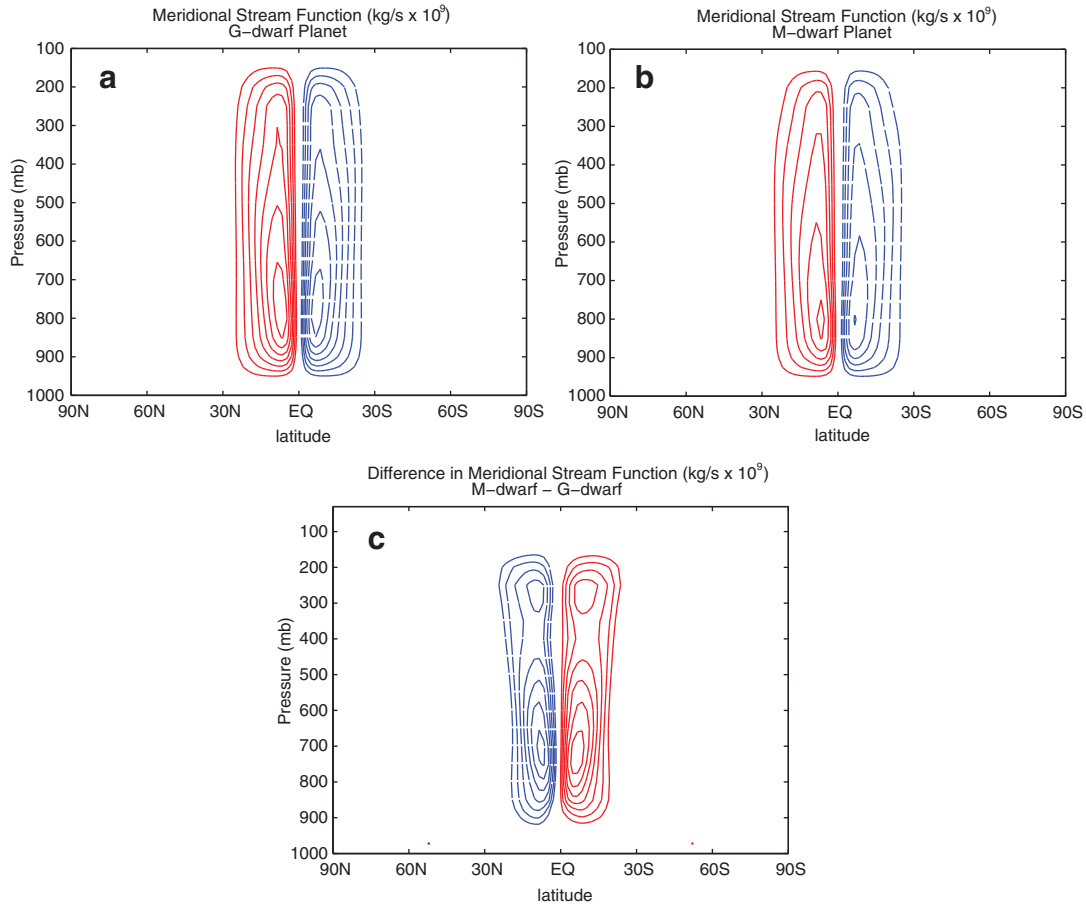

FIG. 12. GCM comparison of an M-dwarf aqua planet receiving 90% of the modern solar constant compared with an aqua planet receiving 100% of the modern solar constant from the Sun, a G-dwarf star. Blue dotted—clockwise circulation. Red—counterclockwise circulation. (**a**) Meridional stream function in the atmosphere of the G-dwarf planet; the contours start at $50\,\mathrm{kg/s}\times10^9$, and the contour interval is $25\,\mathrm{kg/s}\times10^9$. (**b**) Meridional stream function in the atmosphere of the M-dwarf planet; the contours start at $50\,\mathrm{kg/s}\times10^9$, and the contour interval is $25\,\mathrm{kg/s}\times10^9$. (**c**) Increase in the meridional stream function in the atmosphere of the M-dwarf planet, calculated by taking the difference between the M-dwarf planet's meridional stream function and the G-dwarf planet's meridional stream function; the contours start at $10\,\mathrm{kg/s}\times10^9$, and the contour interval is $5\,\mathrm{kg/s}\times10^9$. The weaker Hadley circulation on the M-dwarf planet results in greater atmospheric temperatures, and less heat transported away from the equator, compensating for the reduced instellation relative to the G-dwarf planet. Color images available online at www.liebertonline.com/ast

longer than 1.1 μm. Cross-section and line absorption coefficient files for CO_2 were included as input and created with LBLABC with data from the HITRAN 2008 database (Rothman *et al.*, 2009). The results are plotted in Fig. 18.

The pure nitrogen atmosphere run resulted in the highest broadband planetary albedo due to its relative dearth of spectral absorption features. When 0.1 bar of atmospheric CO_2 is introduced, the broadband planetary albedo decreases by 7%. When the artificially enhanced snow spectrum is used as the input surface spectrum, the broadband albedo values for the pure nitrogen atmosphere case increase by the largest amount. As atmospheric CO_2 concentration is increased, the difference between the calculated broadband planetary albedo for which the actual snow spectrum was used and that for which the artificially higher snow spectrum was used decreases. At atmospheric concentrations of $\sim$3 bar of CO_2, the broadband albedo for the planet with the actual snow spectrum matches that calculated with the artificially high snow spectrum to within 6.5%. At 10 bar of CO_2, the two values match to within two-tenths of 1%. Differences in reflectivity as a function of wavelength between the planets with the actual and altered snow surfaces, given CO_2 concentrations of 0.1, 3, and 10 bar, are shown in Fig. 19. With 10 bar of CO_2 in the atmosphere, the reflectivity at longer wavelengths has plummeted due to near-IR absorption by CO_2, and the spectra of the planets with the actual and artificially enhanced snow albedo spectra are indistinguishable.

The absorption cross section of CO_2 is temperature-dependent, with cross sections increasing with temperature toward longer wavelengths (Parkinson *et al.*, 2003). Increasing the temperature at which our absorption coefficients were calculated in SMART by 50 K for atmospheres of 10 bar of CO_2 resulted in a $\sim$10% decrease in broadband planetary albedo. There is therefore more work to do in the future on the temperature-dependent CO_2 absorption profile and its influence on the snow and ice-albedo effect on M-dwarf planets.

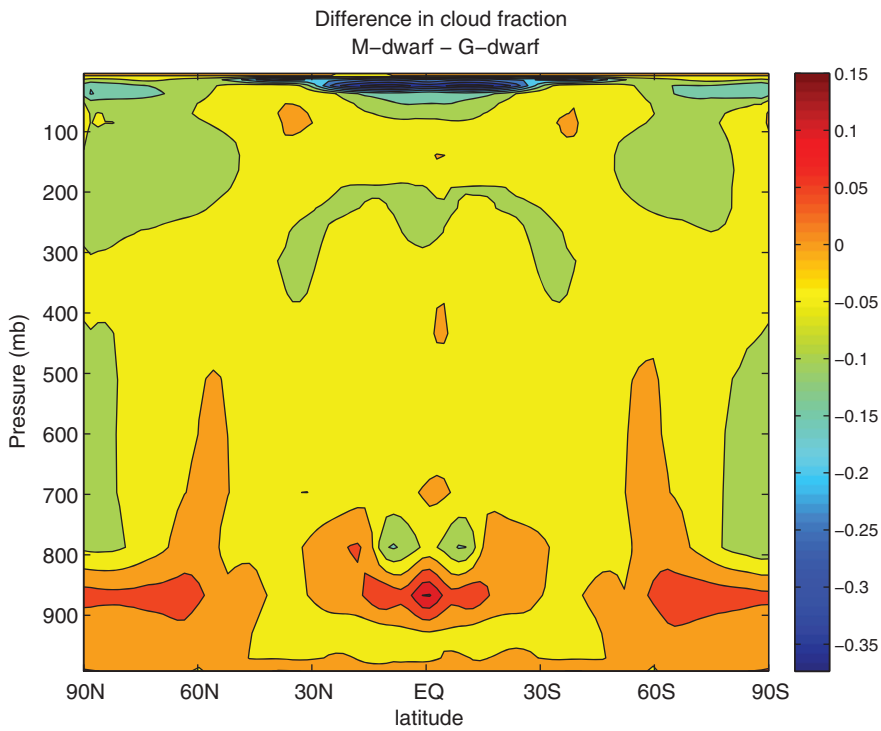

FIG. 13. Difference between the cloud fraction in the atmosphere of an aqua planet receiving 90% of the modern solar constant from an M-dwarf star and an aqua planet receiving 100% of the modern solar constant from the Sun after a 40-year GCM run.

As GCMs are currently incapable of simulating atmospheric CO_2 concentrations greater than $\sim$0.1 bar, we used SMART with our 1-D EBM to address the high-CO_2 case. Figure 20 shows the results of EBM simulations in which we used broadband planetary albedos calculated with SMART assuming a 3-bar pure CO_2 atmosphere on planets orbiting M-, G-, and F-dwarf stars, along with the original EBM simulations with Earth-like atmospheric CO_2 concentrations from Fig. 6. Inputs to SMART, including the atmospheric pressure profile and molecular weight of the atmosphere, were scaled for a 3-bar surface pressure. As in the model runs with an Earth-like atmosphere, broadband planetary albedos for different surface types were generated assuming both clear and cloudy sky conditions. Average broadband planetary albedos over ocean, land, and below-freezing surfaces for the high-CO_2 case were calculated as described in Section 3 and used as input to the EBM. The coefficients governing the effect of CO_2 and water vapor in the linear function of temperature that is parameterized for outgoing longwave radiation in the EBM were also adjusted to account for the increased CO_2. Due to near-IR absorption by the significantly larger amount of CO_2 in the atmospheres of the three planets, ice-free climates exist on all planets with much higher decreases in instellation than in the simulations with an Earth-like CO_2 concentration. Once ice appears on each planet, the ice expands to total ice cover with a smaller reduction in instellation than with Earth-like CO_2 levels, as the planets are close to the OHZ at these low values of stellar flux density. This increased climate sensitivity is the result of much lower surface temperatures at those low values of instellation, as well as the weaker relationship between outgoing longwave radiation and surface temperature in this high-CO_2 case. In essence, the greenhouse effect fails to keep the surface temperature above freezing over large areas of the planet at these low values of instellation as we approach the maximum CO_2 greenhouse limit. Figure 20 indicates that, given high levels of CO_2, planets remain ice-free throughout the majority of the width of the habitable zone. M-dwarf planets with 3 bar of CO_2 in their atmospheres appear ice-free with larger decreases in instellation than G- or F-dwarf planets with equivalent CO_2 concentrations. This is due to greater CO_2 absorption of the increased near-IR radiation emitted by M-dwarf stars. M-dwarf planets appear to be less susceptible to global glaciation over the course of their

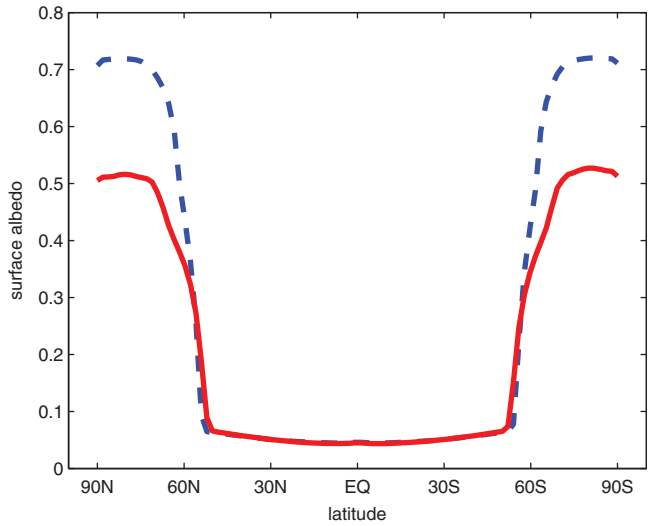

FIG. 14. Surface albedo as a function of latitude for an M-dwarf aqua planet receiving 90% of the modern solar constant (red) compared with an aqua planet receiving 100% of the modern solar constant from the Sun, a G-dwarf star (blue dashed), after a 40-year GCM run.

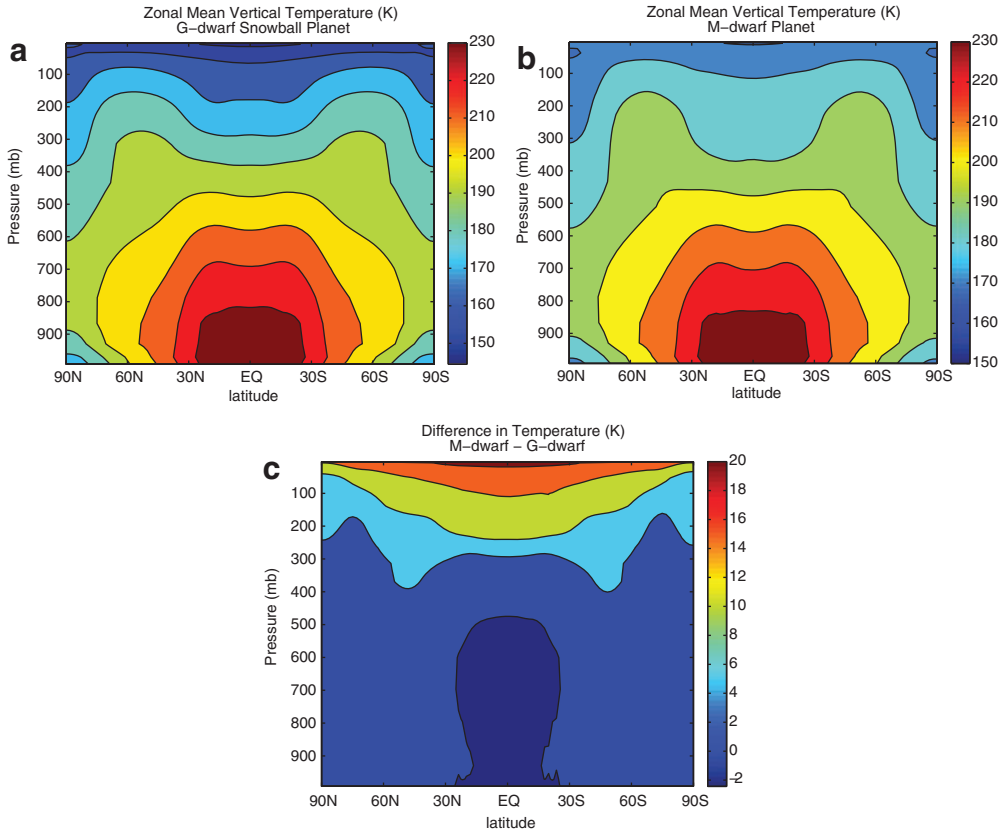

FIG. 15. GCM comparison of an M-dwarf aqua planet receiving 73% of the modern solar constant (993 W/m^2) with an aqua planet orbiting the Sun and receiving 92% of the modern solar constant (1251 W/m^2). Both planets are completely ice-covered. (**a**) Zonal mean temperature in the atmosphere of the G-dwarf planet; (**b**) zonal mean temperature in the atmosphere of the M-dwarf planet; (**c**) increase in temperature in the atmosphere of the M-dwarf aqua planet, calculated by taking the difference between the M-dwarf planet's atmospheric temperature profile and the G-dwarf planet's atmospheric temperature profile.

history, but at the OHZ, where CO_2 levels are expected to be high, the ice-albedo effect is muted by atmospheric CO_2 absorbing strongly in the near IR. Once ice does appear on the planets, even with the largest-grained, lowest-albedo ice surfaces, the points of global ice cover do not occur farther out than the traditional maximum CO_2 greenhouse limits (Kasting *et al.*, 1993), which have been updated by Kopparapu *et al.* (2013a, 2013b). The maximum CO_2 greenhouse limits are plotted as vertical lines for each planet in Fig. 20.

5. Discussion

The results of our model simulations indicate that the interaction between wavelength-dependent planetary surface albedo and the SED of a star may significantly affect the climate of an orbiting planet. The spectral dependence of ice and snow albedo is most important for planets in the middle range of a star's habitable zone. At the IHZ, a planet will receive too much flux to have significant ice on its surface. At the OHZ, high CO_2 masks the ice-albedo effect.

Our SMART + EBM model can reproduce Earth's current global mean surface temperature and ice line latitude at its present obliquity to within 3°C and six degrees of latitude, respectively, given gas absorption by the seven major atmospheric constituent species. EBM simulations produce ice lines that are farther toward the poles on M-dwarf planets compared to those on G-dwarf planets for a given instellation, providing confirmation of the analytical supposition of Joshi and Haberle (2012) that the cooling effect of ice-albedo feedback may indeed be suppressed on planets orbiting stars that emit large amounts of radiation in the near IR, where ice and snow absorb strongly. Building on their initial work, our EBM results additionally imply that the cooling effect of ice-albedo feedback may be enhanced on planets orbiting F-dwarf stars, as global ice cover occurs for a much smaller change in instellation on F-dwarf planets than on planets orbiting G- or M-dwarf stars (Figs. 6 and 8). SMART upwelling and downwelling flux output indicates that broadband planetary albedo increases for SEDs with higher visible and near-UV radiation output, especially for ice and snow surface spectra, whose wavelength-dependent albedo increases in the visible and near UV. This trend remains even when the effect of Rayleigh scattering in the atmosphere is removed and would be absent without incorporating the spectral dependence of ice and snow albedo across the full near-UV through near-IR spectrum. Planets orbiting cooler, redder stars remain free from global ice cover with larger decreases in instellation. This effect may also be reinforced at higher obliquities than those considered here, as previous work has shown that planets with high planetary obliquities

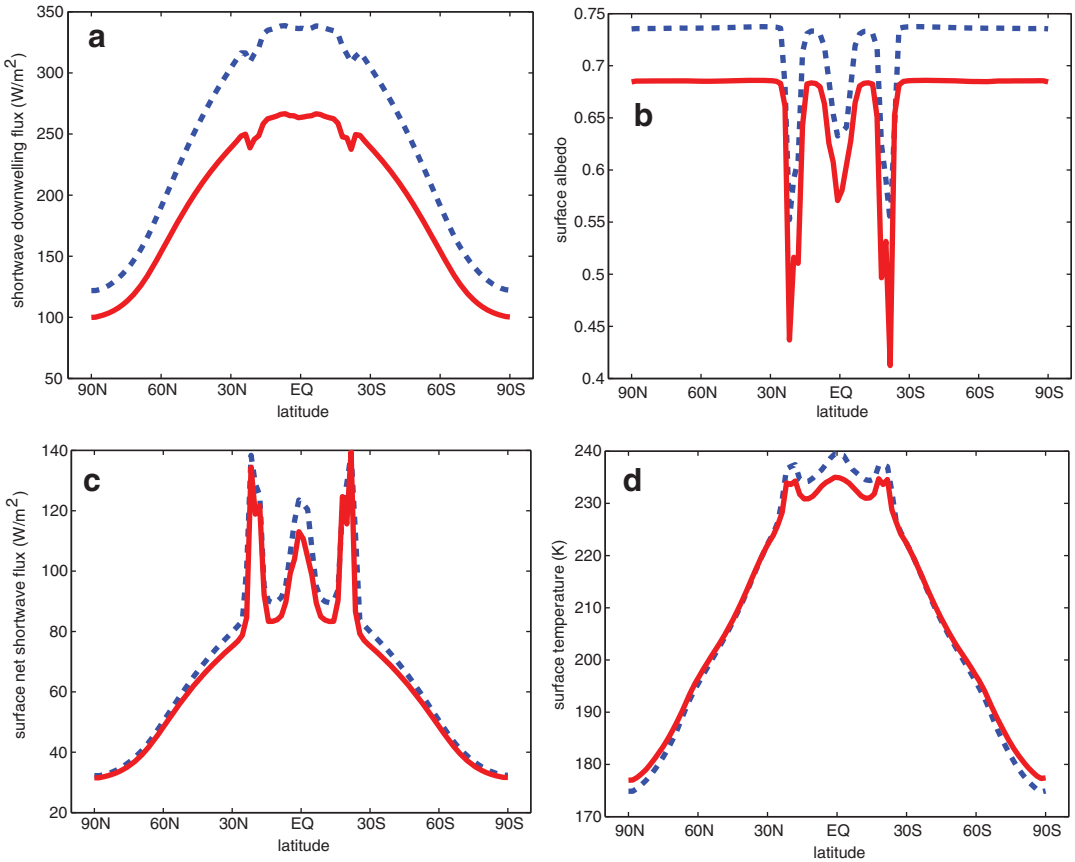

FIG. 16. GCM comparison of an M-dwarf aqua planet (red) receiving 73% of the modern solar constant (993 W/m^2) with an aqua planet orbiting the Sun and receiving 92% of the modern solar constant (1251 W/m^2, blue dashed). Both planets are completely ice-covered. (**a**) Surface shortwave downwelling flux as a function of latitude; (**b**) surface albedo; (**c**) net shortwave flux absorbed by the surface; (**d**) surface temperature. Color images available online at www.liebertonline.com/ast

may be less susceptible to snowball episodes (Williams and Kasting, 1997; Spiegel *et al.*, 2009).

Additionally, we found that ice grain size strongly affects the latitudinal extent of the ice line and that the type of ice on a planetary surface may strongly affect its climate. The larger the ice grain size, the lower the calculated broadband planetary albedo and the higher the resulting ice line latitude determined by the EBM. Given a simplified aqua planet configuration, ice-covered states are possible with smaller decreases in instellation for below-freezing surfaces of finer grain size such as fresh snow, which have high broadband albedos, given an F-dwarf incident spectrum. Assuming an Earth-like atmosphere with clouds and the effect of Rayleigh scattering included, our SMART runs show that increasing the ice grain size results in a $\sim$12% to $\sim$17% increase in broadband planetary albedo per 25% mixture of blue ice and snow. Planets with surfaces composed of ice of larger grain size appear to be more stable against snowball episodes.

To further explore the atmospheric response to instellation of varying SED, we ran 3-D GCM simulations as well. In our GCM runs, we assumed an aqua planet with a 50 m slab ocean. With a 10% reduction in instellation, surface temperatures are warmer on an orbiting M-dwarf aqua planet than a G-dwarf aqua planet, due to greater atmospheric absorption and emission of the large proportion of near-IR radiation from M-dwarf stars, by greenhouse gases like CO_2 and water vapor, which have many absorption bands in the near-IR and IR regions of the spectrum. Therefore, atmospheric absorption and downwelling longwave heating play a large role in reducing the fraction of ice covering M-dwarf planets.

However, the role played by the spectral dependence of ice albedo in affecting climate is not insignificant. In our GCM simulations of M-dwarf planets receiving far less instellation than G-dwarf planets, we found that a higher percentage of absorption by surface ice of the reduced amount of incident shortwave radiation on the M-dwarf planet helps to compensate for the reduced instellation. Lowering the albedos of ice and snow decreased the climate sensitivity of the M-dwarf planet compared to that for which the default albedo values were used. This result implies that increased shortwave absorption by surface ice increases climate stability to changes in instellation, and planetary climate appears to be affected by the spectral dependence of ice albedo, even in the presence of Earth-like greenhouse gases in the atmosphere.

The slopes in Fig. 8 are a measure of the climate sensitivity to changes in instellation for these planets, given their host star SEDs and the concentration of CO_2 held fixed at the present atmospheric level on Earth. They indicate a larger change in ice cover for a given change in instellation for planets with incident spectra like the Sun's or bluer host stars as compared to redder stars. The G-dwarf planet was

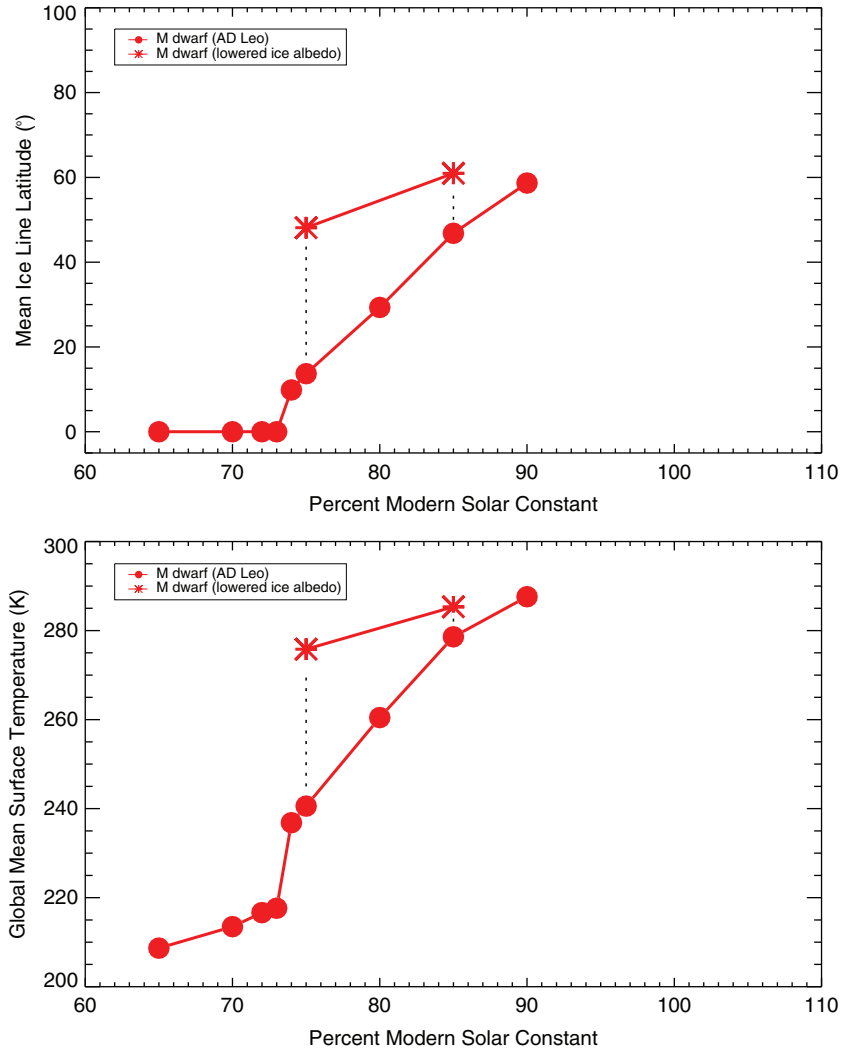

FIG. 17. Mean ice line latitude (top) and global mean surface temperature (bottom) as a function of percent of modern solar constant after a 40-year GCM run for an aqua planet orbiting an M-dwarf star, from Fig. 8. Also plotted here are the resulting ice extents and global mean surface temperatures for M-dwarf planets receiving 75% and 85% instellation, with IR and visible-band ice and snow albedos lowered to 0.2 (asterisks). The difference in climates is larger between the M-dwarf planets receiving 75% instellation than between the M-dwarf planets receiving 85% instellation (as indicated by the black vertical lines), exhibiting a shallower change in global mean surface temperature and ice extent for lowered instellation than with the default albedo parameterization. Color images available online at www.liebertonline.com/ast

entirely frozen over at 92% of the modern solar constant. This result is similar to those of previous climate simulations carried out by Abe *et al.* (2011), who found that an aqua planet around the Sun becomes ice-covered with a 10% reduction in instellation. A snowball state was not reached in our GCM simulations of an M-dwarf planet until the amount of flux from the star was reduced to 73% of the modern solar constant. An F-dwarf planet was completely frozen over with only a 2% reduction in instellation compared to that of present-day Earth. M-dwarf planets therefore appear much less sensitive to changes in instellation and thus less susceptible to snowball states. The Neoproterozoic Snowball Earth episodes of ~750 to ~635 million years ago have been linked to the emergence of multicellular life on Earth due to enhancement of the flux of dissolved phosphates into the ocean, which would have caused increased primary productivity and organic carbon burial and led to the rise of oxygen in the ocean and atmosphere (Planavsky *et al.*, 2010). Planets less likely to experience such global-scale glaciations may therefore be dependent on alternate pathways to serve as catalysts for biological evolution. The M-dwarf planet in our simulations also exhibited more stable lower-latitude ice lines than the G- or F-dwarf planets; this may be due to the lower-albedo ice formed on its surface. A more stable low-latitude ice line on M-dwarf planets may be possible as the result of a lower albedo contrast between bare sea ice and snow-covered ice (Abbot *et al.*, 2011).

Land planets orbiting Sun-like stars, given their lower thermal inertia and drier atmospheres, completely freeze with a 23% reduction in instellation, to 77% of the modern solar constant (Abe *et al.*, 2011). Given that M-dwarf aqua planets continue to exhibit ice-free areas until their stellar flux has been reduced by 27% (to 73% of the modern solar constant), M-dwarf planets may be more resistant to freezing than G-dwarf planets, regardless of land percentage.

5.1. Additional factors affecting planetary climate

We assumed a rotation period equal to present-day Earth (24 h) for our simulations to isolate the effect of stellar SED and ice-albedo feedback on planetary climate. Synchronous rotation, which is expected to occur on M-dwarf planets orbiting in their stars' habitable zones (Dole, 1964; Kasting *et al.*, 1993; Joshi *et al.*, 1997; Edson *et al.*, 2011), would certainly affect the results presented here. Earlier work by Edson *et al.* (2011) indicates that increasing the rotation period

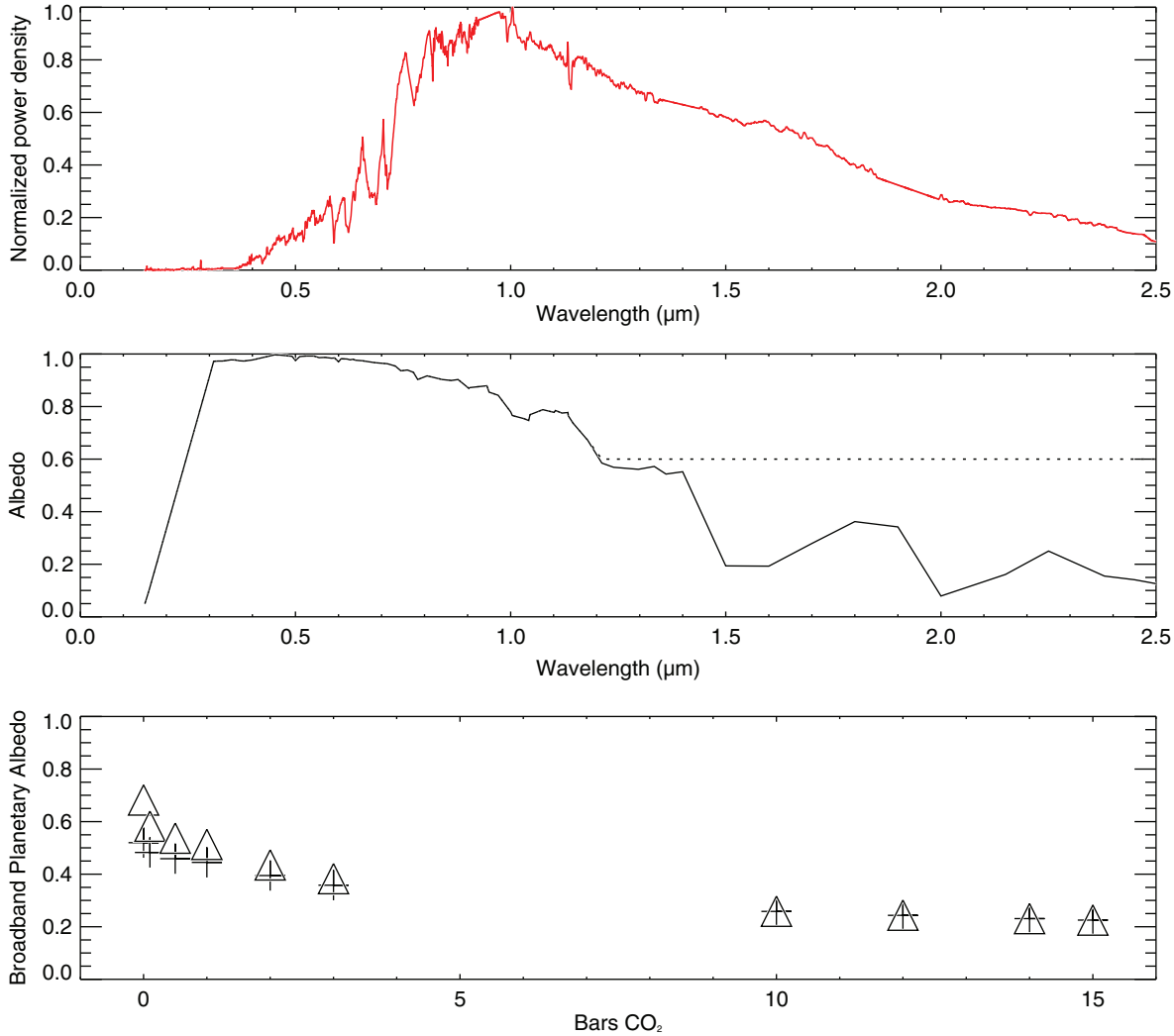

FIG. 18. Top: The normalized SED of the M3V star AD Leo. Middle: The albedo spectrum of fine-grained snow (solid line), with artificially enhanced albedo values of 0.6 at wavelengths longer than 1.1 μm (dashed line). Bottom: Broadband planetary albedos ($0.15\,\mu m \leq \lambda \leq 2.5\,\mu m$) as output from SMART, given an incident M-dwarf spectrum, input actual (plus symbols) and artificially enhanced (triangles) snow albedo spectra, and various concentrations of atmospheric CO_2. The concentration of CO_2 can be expected to effectively mask the ice-albedo spectral dependence when the broadband planetary albedo for the actual input snow spectrum (with lower near-IR albedo values) matches that for the artificially enhanced snow spectrum (with high values of near-IR albedo), demonstrating that broadband planetary albedo is no longer sensitive to the surface albedo of the planet. This appears to happen at atmospheric concentrations of between 3 and 10 bar of CO_2. Color images available online at www.liebertonline.com/ast

of an aqua planet weakens low-latitude zonal winds and cools the planet, and increased atmospheric latent and oceanic diffusive heat transport could reduce temperature contrasts between the sunlit and dark sides of the planet. Given that a solar-type spectrum was used in their work, and our work here with an M-dwarf spectrum results in greater surface temperatures on M-dwarf planets than on G-dwarf planets that receive equal amounts of instellation, temperature contrasts between the sunlit and dark sides of a synchronously rotating aqua planet orbiting an M-dwarf star at a 1 AU equivalent flux distance may be even further reduced.

Previous studies that used GCM simulations of synchronously rotating planets at 1 AU equivalent flux distances from a solar-type star suggest that atmospheric CO_2 concentrations could be nearly 200 times higher than the present atmospheric level on Earth if the substellar point is over a predominantly ocean-covered area, due to a lack of continental weathering (Edson *et al.*, 2012). However, atmospheric CO_2 concentration could be limited by seafloor weathering on an aqua planet, resulting in much lower CO_2 partial pressures (Edson *et al.*, 2012). Here, we have simulated an M-dwarf aqua planet with a 24 h rotation period, making an Earth-like atmospheric CO_2 concentration a reasonable assumption.

Although M-dwarf planet climates appear to be sensitive to the surface at present atmospheric levels of CO_2, there is a limit to the amount of CO_2 that can exist in the atmosphere of a planet without masking the surface entirely at near-IR wavelengths. The SED of M-dwarf stars coupled with the spectral dependence of ice and snow albedo may indeed allow M-dwarf planets to exist "snowball free" with larger decreases in instellation than planets orbiting stars with

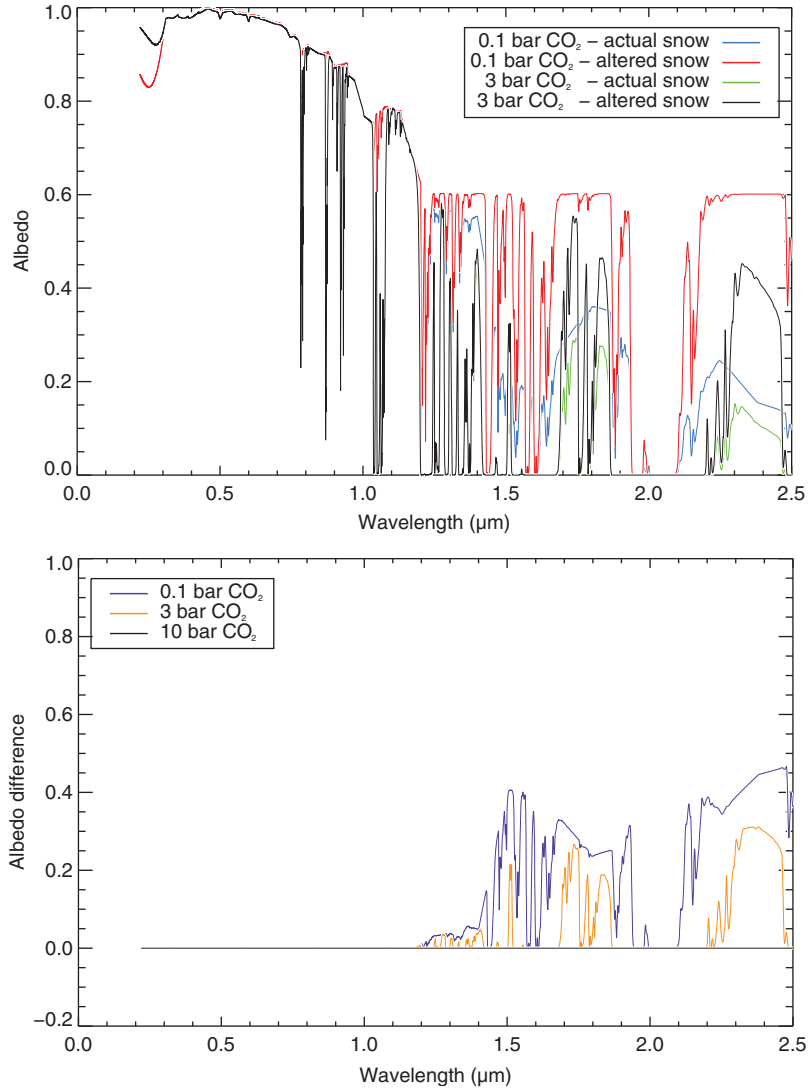

FIG. 19. Wavelength-dependent reflectivity of a planet with various concentrations of atmospheric CO_2 and an underlying snow surface, calculated with SMART and the actual measured albedo spectrum, and one that was altered to exhibit artificially high albedo values of 0.6 at wavelengths longer than 1.1 μm. Top: 0.1 bar of CO_2 and an underlying snow surface matching the fine-grained snow spectrum in Fig. 1 (blue); 0.1 bar of CO_2 with a snow surface with an artificially enhanced spectrum (red); 3-bar CO_2 atmosphere with the actual snow spectrum (green); 3-bar CO_2 atmosphere with the artificially enhanced snow spectrum (black). Bottom: Change in reflectivity between the planets with artificially enhanced vs. actual snow surface albedo spectra. With 3 bar of CO_2 in the atmosphere, the difference between the albedos of the planets (orange) has decreased significantly compared to that of the 0.1-bar planets (purple). With 10 bar of CO_2 in the atmosphere, the difference in the albedo spectra of the planets (black) is close to zero, due to increased near-IR absorption by CO_2 at longer wavelengths.

higher visible and near-UV output, assuming low to moderate atmospheric levels of CO_2. However, CO_2 can be expected to build up in the atmosphere in response to lower surface temperatures and decreased silicate weathering (Walker *et al.*, 1981). Abbot *et al.* (2012) found that, provided the land fraction is at least $\sim$0.01, climate weathering feedback should operate without a strong dependence on land fraction. As our EBM simulations with high-CO_2 atmospheres used a land fraction of 0.01 (Section 2.2), to assume a high-CO_2 atmosphere that could result from climate weathering feedback at the OHZ is not unreasonable.

The high-CO_2 atmospheres (>3–10 bar) we simulated using SMART may be sufficient to mask the suppressed ice-albedo feedback that is expected to occur on M-dwarf planets. From our EBM simulations of planets with 3-bar pure CO_2 atmospheres, the increased absorption of near-IR radiation by large amounts of CO_2 prevents ice from forming on all three planets with significantly larger decreases in instellation than in the simulations with Earth-like CO_2 levels. The increased climate sensitivity that occurs once ice does appear on a planet with 3 bar of CO_2 in its atmosphere is the result of the greenhouse effect failing to keep surface temperatures above freezing at low values of instellation near the OHZ. We would expect to see this behavior persist in GCM simulations as well. Climate model simulations of Earth-like planets at the outer edge of their stars' habitable zones, with CO_2 partial pressures of 3–10 bar, are outside the realm of present GCM capabilities.

Higher concentrations of CO_2 appear to lower the calculated broadband albedo of planets with M-dwarf host stars (though the amount of reduced albedo decreases as CO_2 increases, as indicated by the flattening of the curve in Fig. 18, bottom). For M-dwarf host stars, this may be largely due to increased CO_2 atmospheric absorption in the near IR. However, increased Rayleigh scattering due to high CO_2 concentrations is expected to lead to increases in planetary albedo, at least for G-dwarf host stars such as the Sun (Kasting and Ackerman, 1986). The effect of Rayleigh scattering could dominate atmospheric absorption at higher pressures. However, given that the effect of Rayleigh scattering is more pronounced for shorter-wavelength incident radiation, our decreased planetary albedos for higher-pressure atmospheres may be the consequence of atmospheric absorption masking high-albedo snow, given that Rayleigh scattering is less important on planets that receive higher percentages of long-wavelength radiation from their

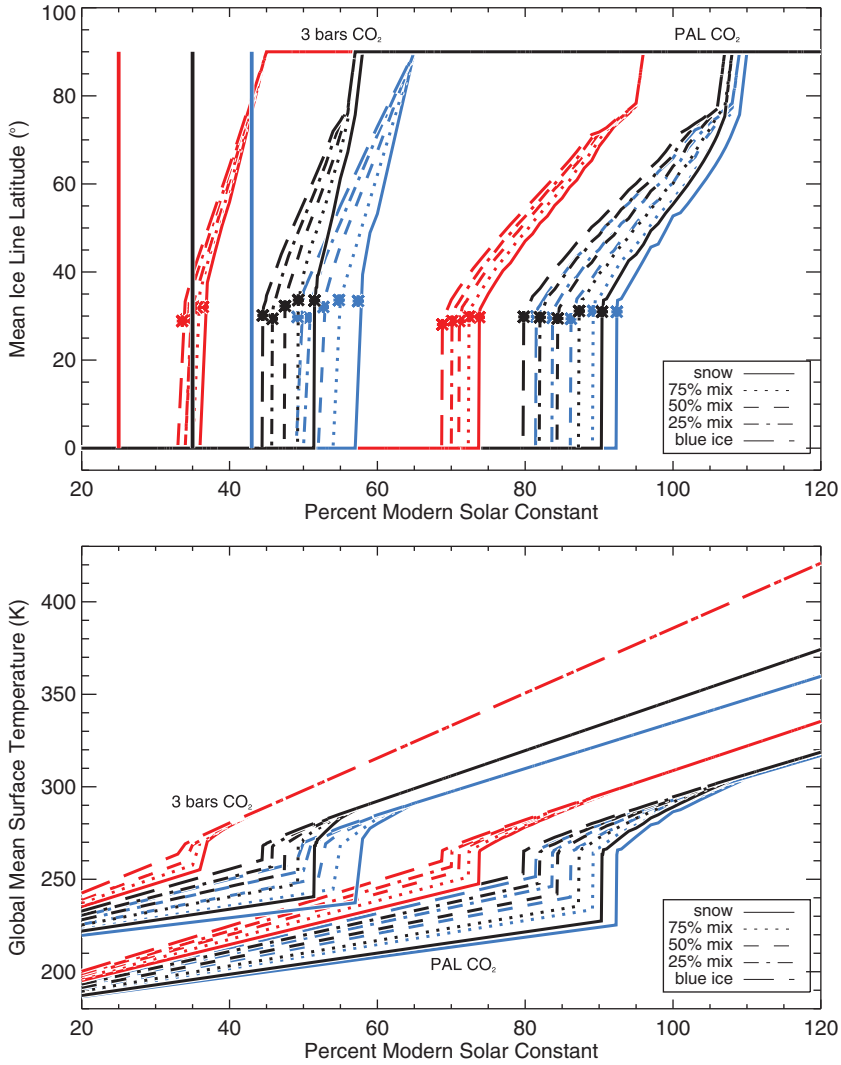

FIG. 20. Mean ice line latitude (top) and global mean surface temperature (bottom) in the northern hemisphere as a function of percent of modern solar constant are calculated using a seasonal EBM, at present Earth obliquity (23.5°) for aqua planets (land and ocean fraction 0.01 and 0.99, respectively) orbiting F-, G-, and M-dwarf stars at an equivalent flux distance, as in Fig. 6. Here the present atmospheric level (PAL) of CO_2 as well as 3 bar of CO_2 were used (F-dwarf planet in blue, G-dwarf planet in black, and M-dwarf planet in red). Asterisks denote the minimum ice line latitude before collapse to the equator and global ice coverage. Also plotted here as vertical solid lines are the updated maximum CO_2 greenhouse limits for the F-dwarf (blue), G-dwarf (black), and M-dwarf (red) planets (Kopparapu *et al.*, 2013a, 2013b).

host stars (Kasting *et al.*, 1993; Pierrehumbert, 2011; Kopparapu *et al.*, 2013a). There may therefore be a particular stellar mass (somewhere between AD Leo and the Sun) above which the combined effects of Rayleigh scattering and atmospheric near-IR absorption are maximized. Indeed, we found that the broadband albedo of a K-dwarf planet also decreased with higher concentrations of CO_2, and by a smaller percentage than that of our M-dwarf planet. Here, we assumed a 1 AU equivalent flux distance for the M-dwarf planet, so the likelihood of CO_2 cloud formation in the atmosphere was low. Previous work with a 1-D radiative-convective model has suggested that CO_2 ice clouds in the atmosphere may result in net warming of a planet's surface (Forget and Pierrehumbert, 1997).

Given that the silicate weathering thermostat adjusts the CO_2 concentration to increase with decreasing surface temperature and M-dwarf planets appear to be less sensitive to changes in instellation (as indicated by the shallower change in temperature and ice extent on the M-dwarf planet shown in Figs. 6 and 8), habitable M-dwarf planets can be expected to exhibit lower concentrations of CO_2 at a given distance from their host stars than planets orbiting stars with higher visible and near-UV output. Essentially, lower amounts of CO_2 are required for an M-dwarf planet to remain free of global ice-cover at lower values of instellation. We have not explored with a GCM the effect of decreased CO_2 on the percent of the modern solar constant required for global ice cover on an M-dwarf planet. Given the increased atmospheric stability in the troposphere of the M-dwarf planet receiving 73% of the modern solar constant compared to the G-dwarf planet receiving 92% of the modern solar constant (Fig. 15), we expect the M-dwarf planet to be more resistant to global glaciation with decreased CO_2 than a G-dwarf planet, given an equivalent reduction in atmospheric CO_2 concentration. The difference between M-dwarf planets and planets orbiting hotter main-sequence stars becomes less noticeable at the OHZ (where the masking effect of high CO_2 becomes more important) than closer in to the star (where CO_2 levels would be lower, and more ice would form on a planet's surface).

Our EBM simulations with 3-bar CO_2 atmospheres indicate that the spectral dependence of surface ice albedo is less important at the OHZ, as planets remain free of ice cover throughout the majority of the width of the habitable zone due to large amounts of near-IR absorption by CO_2. We found that M-dwarf planets become ice-covered at $\sim$33% of

the modern solar constant with 3 bar of CO_2 in their atmospheres, given the lowest-albedo ice surface. This value, while much smaller than that required for ice-covered conditions given Earth-like CO_2 levels (73% of the modern solar constant, from our GCM results), is still greater than the maximum CO_2 greenhouse limit, derived by Kasting *et al.* (1993) and updated by Kopparapu *et al.* (2013a, 2013b), of 25% of the modern solar constant for a planet orbiting an M0 star. It has been postulated that the OHZ may be 10–30% farther out from an M-dwarf star given the effect of the wavelength-dependent reflectivity of surface ice and snow on planetary albedo (Joshi and Haberle, 2012). However, CO_2 partial pressures of 10 bar or more may be required to maintain atmospheric stability and surface liquid water at the OHZ for M-dwarf stars (Wordsworth *et al.*, 2011), and we have shown that high levels of atmospheric CO_2 entirely mask the climatic effect of surface water ice and snow. Therefore, we find the traditional OHZ to be unaffected by the spectral dependence of ice and snow albedo.

6. Conclusions

Using 1-D and 3-D climate simulations, we demonstrated that planets orbiting cooler, redder stars at equivalent flux distances exhibit higher global mean surface temperatures than planets orbiting stars with more visible and near-UV radiation output. The increased surface temperatures are in large part the consequence of absorption by atmospheric gases of the significantly higher percentage of near-IR radiation emitted by M-dwarf stars. However, we have shown that the spectral dependence of water ice and snow albedo does play a role in affecting climate. Changes to planetary climate appear to be less sensitive to M-dwarf SED than G- and F-dwarf SED, as evidenced by the smaller change in ice extent for a given change in stellar flux for M-dwarf planets. At a fixed level of CO_2, M-dwarf aqua planets remain free of global ice cover with 25% less stellar flux than F-dwarf aqua planets and 19% less stellar flux than G-dwarf aqua planets. M-dwarf planets may therefore be more stable against low-latitude glaciation over the course of their history than planets orbiting stars with higher visible and near-UV radiation output. As low-latitude glaciation has been linked to the emergence of complex life on Earth, planets less predisposed to such glacial episodes would need to rely on other means to aid in biological evolution. M-dwarf planets may also exhibit more stable low-latitude ice lines as a consequence of lower-albedo ice on their surfaces. At the OHZ, where CO_2 can be expected to increase with decreasing surface temperature and silicate weathering, the spectral dependence of surface ice and snow albedo is less important and does not extend the traditional OHZ given by the maximum CO_2 greenhouse. However, due to their lower climate sensitivity to changes in instellation, M-dwarf planets would likely have lower amounts of CO_2 in their atmospheres far out in their stars' habitable zones than planets orbiting stars with higher visible and near-UV output at an equivalent flux distance, and they would require less CO_2 to maintain clement conditions for surface liquid water.

Acknowledgments

This material is based upon work supported by the National Science Foundation Graduate Research Fellowship Program under grant Nos. DGE-0718124 and DGE-1256082. This work was performed as part of the NASA Astrobiology Institute's Virtual Planetary Laboratory Lead Team, supported by the National Aeronautics and Space Administration through the NASA Astrobiology Institute under Cooperative Agreement solicitation NNH05ZDA001C. The authors wish to thank two anonymous referees for their comments and suggestions, which greatly improved the paper. A.L.S. thanks David Crisp and Amit Misra for useful conversations about F-dwarf stars, ozone, and SMART; Eric Agol for help with stellar flux calculations; John Armstrong for helpful IDL stellar interpolation code; and John Johnson and Carl Grillmair for helpful advice regarding graphics. Special thanks to the Virtual Planet Laboratory for computer models and resources, the NASA Astrobiology Institute, the NSF Astrobiology IGERT program, Bruce Briegleb, and Tom Ackerman. Daniel Koll provided assistance with running the GCM in aqua planet mode. Stephen Warren provided advice about spectral albedos of snow and ice.

Author Disclosure Statement

No competing financial interests exist.

Abbreviations

CAM4.0, Community Atmosphere Model version 4; CCSM, Community Climate System Model; EBM, energy balance model; GCM, general circulation model; ICRCCM, Intercomparison of Radiation Codes in Climate Models program; IHZ, inner edge of the habitable zone; LBLABC, line-by-line absorption coefficient model; OHZ, outer edge of the habitable zone; SED, spectral energy distribution; SMART, Spectral Mapping Atmospheric Radiative Transfer model.

References

Abbot, D.S., Voigt, A., and Koll, D. (2011) The Jormungand global climate state and implications for Neoproterozoic glaciations. *J Geophys Res* 116, doi:10.1029/2011JD015927.

Abbot, D.S., Cowan, N.B., and Ciesla, F.J. (2012) Indication of insensitivity of planetary weathering behavior and habitable zone to surface land fraction. *Astrophys J* 756, doi:10.1088/0004-637X/756/2/178.

Abe, Y., Abe-Ouchi, A., Sleep, N.H., and Zahnle, K.J. (2011) Habitable zone limits for dry planets. *Astrobiology* 11:443–460.

Barkstrom, B.R. and Hall, J.B. (1982) Earth Radiation Budget Experiment (ERBE)—an overview. *Journal of Energy* 2:141–146.

Bitz, C.M., Shell, K.M., Gent, P.R., Bailey, D.A., Danabasoglu, G., Armour, K.C., Holland, M.M., and Kiehl, J.T. (2012) Climate sensitivity of the Community Climate System Model, version 4. *J Clim* 25:3053–3070.

Borucki, W.J. and Summers, A.L. (1984) The photometric method of detecting other planetary systems. *Icarus* 58:121–134.

Brandt, R.E., Warren, S.G., Worby, A.P., and Grenfell, T.C. (2005) Surface albedo of the Antarctic sea ice zone. *J Clim* 18:3606–3622.

Budyko, M.I. (1969) The effect of solar radiation variations on the climate of the Earth. *Tellus* 21:611–619.

Chance, K. and Kurucz, R.L. (2010) An improved high-resolution solar reference spectrum for Earth's atmosphere measurements in the ultraviolet, visible, and near infrared. *J Quant Spectrosc Radiat Transf* 111:1289–1295.

Crisp, D. (1997) Absorption of sunlight by water vapor in cloudy conditions: a partial explanation for the cloud absorption anomaly. *Geophys Res Lett* 24:571–574.

Dole, S.H. (1964) *Habitable Planets for Man*, Blaisdell, New York.

Dunkle, R.V. and Bevans, J.T. (1956) An approximate analysis of the solar reflectance and transmittance of a snow cover. *Journal of Meteorology* 13:212–216.

Edson, A., Lee, S., Bannon, P., Kasting, J.F., and Pollard, D. (2011) Atmospheric circulations of terrestrial planets orbiting low-mass stars. *Icarus* 212:1–13.

Edson, A.R., Kasting, J.F., Pollard, D., Lee, S., and Bannon, P.R. (2012) The carbonate-silicate cycle and CO_2/climate feedbacks on tidally locked terrestrial planets. *Astrobiology* 12:562–571.

Farrell, E.F. and Newnham, R.E. (1967) Electronic and vibrational absorption in cordierite. *Am Mineral* 52:380–388.

Forget, F. and Pierrehumbert, R.T. (1997) Warming early Mars with carbon dioxide clouds that scatter infrared radiation. *Science* 278:1273–1276.

Gent, P.R., Danabasoglu, G., Donner, L.J., Holland, M.M., Hunke, E.C., Jayne, S.R., Lawrence, D.M., Neale, R.B., Rasch, P.J., Vertenstein, M., Worley, P.H., Yang, Z., and Zhang, M. (2011) The Community Climate System Model version 4. *J Clim* 24:4973–4991.

Grenfell, T.C., Warren, S.G., and Mullen, P.C. (1994) Reflection of solar radiation by the Antarctic snow surface at ultraviolet, visible, and near-infrared wavelengths. *J Geophys Res* 99: 18669–18684.

Hartmann, H. (1994) *Global Physical Climatology,* Academic Press, San Diego.

Hawley, S.L. and Pettersen, B.R. (1991) The great flare of 1985 April 12 on AD Leonis. *Astrophys J* 378:725–741.

Hunke, E.C. and Lipscomb, W.H. (2008) CICE: the Los Alamos sea ice model. Documentation and software, version 4.0. Los Alamos National Laboratory Technical Report LA-CC-06-012, Los Alamos National Laboratory, Los Alamos, NM.

Joshi, M.M. and Haberle, R.M. (2012) Suppression of the water ice and snow albedo feedback on planets orbiting red dwarf stars and the subsequent widening of the habitable zone. *Astrobiology* 12:3–8.

Joshi, M.M., Haberle, R.M., and Reynolds, R.T. (1997) Simulations of the atmospheres of synchronously rotating terrestrial planets orbiting M dwarfs: conditions for atmospheric collapse and the implications for habitability. *Icarus* 129:450–465.

Kane, S.R. and Gelino, D.M. (2012) The habitable zone gallery. *Publ Astron Soc Pac* 124:323–328.

Kasting, J.F. and Ackerman, T.P. (1986) Climatic consequences of very high carbon dioxide levels in the Earth's early atmosphere. *Science* 234:1383–1385.

Kasting, J.F., Whitmire, D.P., and Reynolds, R.T. (1993) Habitable zones around main sequence stars. *Icarus* 101:108–128.

Kirschvink, J. (1992) Late Proterozoic low-latitude global glaciation: the Snowball Earth. In *The Proterozoic Biosphere: A Multidisciplinary Study,* edited by J.W. Schopf, C. Klein, and D. Des Maris, Cambridge University Press, Cambridge, UK, pp 51–52.

Kopparapu, R.K., Ramirez, R., Kasting, J.F., Eymet, V., Robinson, T.D., Mahadevan, S., Terrien, R.C., Domagal-Goldman, S., Meadows, V., and Deshpande, R. (2013a) Habitable zones around main-sequence stars: new estimates. *Astrophys J* 765, doi:10.1088/0004-637X/765/2/131.

Kopparapu, R.K., Ramirez, R., Kasting, J.F., Eymet, V., Robinson, T.D., Mahadevan, S., Terrien, R.C., Domagal-Goldman, S., Meadows, V., and Deshpande, R. (2013b) Erratum: "Habitable zones around main-sequence stars: new estimates." *Astrophys J* 770, doi:10.1088/0004-637X/770/1/82.

Kukla, G. (1979) Climatic role of snow covers. In *Sea Level, Ice, and Climatic Change,* Proceedings of the Canberra Symposium, International Association of Hydrological Sciences Publication 131, p 79–107.

Lindzen, R.S. and Farrell, B. (1977) Some realistic modifications of simple climate models. *J Atmos Sci* 34:1487–1501.

Meadows, V.S. and Crisp, D. (1996) Ground-based near-infrared observations of the Venus nightside: the thermal structure and water abundance near the surface. *J Geophys Res* 101:4595–4622.

Mernild, S.H., Liston, G.E., Hiemstra, C.A., and Christensen, J.H. (2010) Greenland ice sheet surface mass-balance modeling in a 131-yr perspective, 1950–2080. *Journal of Hydrometeorology* 11:3–25.

North, G.R. and Coakley, J.A. (1979) Differences between seasonal and mean annual energy balance model calculations of climate and climate sensitivity. *Journal of Atmospheric Sciences* 36:1189–1204.

Oreopoulos, L. and Khairoutdinov, M. (2003) Overlap properties of clouds generated by a cloud-resolving model. *J Geohpys Res* 108, doi:10.1029/2002JD003329.

Parkinson, W.H., Rufus, J., and Yohino, K. (2003) Absolute absorption cross section measurements of CO_2 in the wavelength region 163–200 nm and the temperature dependence. *Chem Phys* 290:251–256.

Pierrehumbert, R.T. (2010) *Principles of Planetary Climate,* Cambridge University Press, Cambridge, UK.

Pierrehumbert, R.T. (2011) A palette of climates for Gliese 581g. *Astrophys J* 726, doi:10.1088/2041-8205/726/1/L8.

Pierrehumbert, R.T., Abbot, D.S., Voigt, A., and Koll, D. (2011) Climate of the Neoproterozoic. *Annu Rev Earth Planet Sci* 39:417–460.

Planavsky, N.J., Rouxel, O.J., Bekker, A., Lalonde, S.V., Konhauser, K.O., Reinhard, C.T., and Lyons, T.W. (2010) The evolution of the marine phosphate reservoir. *Nature* 467:1088–1090.

Pollard, D. and Kasting, J.F. (2005) Snowball Earth: a thin-ice solution with flowing sea glaciers. *J Geophys Res* 110, doi:10.1029/2004JC002525.

Poulsen, C.J., Pierrehumbert, R.T., and Jacob, R.L. (2001) Impact of ocean dynamics on the simulation of the Neoproterozoic "Snowball Earth." *Geophys Res Lett* 28:1575–1578.

Reid, I.N., Hawley, S.L., and Gizis, J.E. (1995) The Palomar/MSU Nearby-Star Spectroscopic Survey. I. The northern M dwarfs—bandstrengths and kinematics. *Astron J* 110:1838–1859.

Robinson, T.D., Meadows, V.S., Crisp, D., Deming, D., A'Hearn, M.F., Charbonneau, D., Livengood, T.A., Seager, S., Barry, R.K., Hearty, T., Hewagama, T., Lisse, C.M., McFadden, L.A., and Wellnitz, D.D. (2011) Earth as an extrasolar planet: Earth model validation using EPOXI Earth observations. *Astrobiology* 11:393–408.

Rothman, L.S., Gordon, I.E., Barbe, A., Benner, D.C., Bernath, P.F., Birk, M., Boudon, V., Brown, L.R., Campargue, A., Champion, J.P., Chance, K., Coudert, L.H., Dana, V., and Devi, V.M. (2009) The HITRAN 2008 molecular spectroscopic database. *J Quant Spectrosc Radiat Transf* 110:533–572.

Segelstein, D. (1981) The complex refractive index of water. Master's thesis, Department of Physics, University of Missouri–Kansas City, Kansas City, MO.

Segura, A., Krelove, K., Kasting, J.F., Sommerlatt, D., Meadows, V., Crisp, D., Cohen, M., and Mlawer, E. (2003) Ozone con-

centrations and ultraviolet fluxes on Earth-like planets around other stars. *Astrobiology* 3:689–708.

Segura, A., Kasting, J.F., Meadows, V., Cohen, M., Scalo, J., Crisp, D., Butler, R.A.H., and Tinetti, G. (2005) Biosignatures from Earth-like planets around M dwarfs. *Astrobiology* 5:706–725.

Segura, A., Walkowicz, L.M., Meadows, V., Kasting, J., and Hawley, S. (2010) The effect of a strong stellar flare on the atmospheric chemistry of an Earth-like planet orbiting an M dwarf. *Astrobiology* 10:751–771.

Selsis, F., Kasting, J.F., Levrard, B., Paillet, J., Ribas, I., and Delfosse, X. (2007) Habitable planets around the star Gliese 581? *Astron Astrophys* 476:1373–1387.

Spiegel, D.S., Menou, K., and Scharf, C.A. (2009) Habitable climates: the influence of obliquity. *Astrophys J* 691:596–610.

Tarter, J.C., Backus, P.R., Mancinelli, R.L., Aurnou, J.M., Backman, D.E., Basri, G.S., Boss, A.P., Clarke, A., Deming, D., Doyle, L.R., Feigelson, E.D., Freund, F., Grinspoon, D.H., Haberle, R.M., Hauck, S.A., II, Heath, M.J., Henry, T.J., Hollingsworth, J.L., Joshi, M.M., Kilston, S., Liu, M.C., Meikle, E., Reid, I.N., Rothschild, L.J., Scalo, J., Segura, A., Tang, C.M., Tiedje, J.M., Turnbull, M.C., Walkowicz, L.M., Weber, A.L., and Young, R.E. (2007) A reappraisal of the habitability of planets around M dwarf stars. *Astrobiology* 7:30–65.

Underwood, D.R., Jones, B.W., and Sleep, P.N. (2003) The evolution of habitable zones during stellar lifetimes and its implications on the search for extraterrestrial life. *International Journal of Astrobiology* 2:289–299.

Walker, J.C.G., Hays, P.B., and Kasting, J.F. (1981) A negative feedback mechanism for the long-term stabilization of the Earth's surface temperature. *J Geophys Res* 86:9776–9782.

Warren, S.G. and Hahn, C.J. (2002) Cloud climatology. In *Encyclopedia of Atmospheric Sciences*, Oxford University Press, Oxford, pp 476–483.

Warren, S.G., Brandt, R.E., Grenfell, T.C., and McKay, C.P. (2002) Snowball Earth: ice thickness on the tropical ocean. *J Geophys Res* 107:3167–3185.

Williams, D.M. and Kasting, J.F. (1997) Habitable planets with high obliquities. *Icarus* 129:254–267.

Wiscombe, W.J. and Warren, S.G. (1980) A model for the spectral albedo of snow. I: pure snow. *Journal of Atmospheric Sciences* 37:2712–2733.

Wordsworth, R.D., Forget, F., Selsis, F., Millour, E., Charnay, B., and Madeleine, J.-B. (2011) Gliese 581d is the first discovered terrestrial-mass exoplanet in the habitable zone. *Astrophys J* 733, doi:10.1088/2041-8205/733/2/L48.

Zsom, A., Kaltenegger, L., and Goldblatt, C. (2012) A 1D microphysical cloud model for Earth, and Earth-like exoplanets: liquid water and water ice clouds in the convective troposphere. *Icarus* 221:603–616.

Address correspondence to:
Aomawa Shields
Department of Astronomy
University of Washington
Box 351580
Seattle, WA 98195-1580

E-mail: aomawa@astro.washington.edu

Submitted 23 December 2012
Accepted 25 May 2013